Title: Cell-type-specific plasticity in synaptic, intrinsic, and sound response properties of deep-layer auditory cortical neurons after noise trauma

Authors: Yanjun Zhao[1,4,!], Stylianos Kouvaros[1,4,7,!], Nathan A. Schneider[1,4-6], Rebecca F. Krall[1,4], Stephanie Lam[3], Megan P. Arnold[1,4], Ross S. Williamson[1-6*], and Thanos Tzounopoulos[1,2,4*]

[1]Department of Otolaryngology, University of Pittsburgh, Pittsburgh, PA
[2]Department of Neurobiology, University of Pittsburgh, Pittsburgh, PA
[3]Department of Bioengineering, University of Pittsburgh, Pittsburgh PA
[4]Pittsburgh Hearing Research Center, University of Pittsburgh, Pittsburgh, PA
[5]Center for the Neural Basis of Cognition, University of Pittsburgh, Pittsburgh, PA
[6]Center for Neuroscience, University of Pittsburgh, Pittsburgh, PA
[7]Department of Biomedicine, University of Basel, Basel, CH
! These authors contributed equally

[*]To whom correspondence should be addressed:
Ross S. Williamson, PhD:
W1448 Biomedical Science Tower, 200 Lothrop Street, Pittsburgh, PA 15213
Email: rsw@pitt.edu

Thanos Tzounopoulos, PhD:
3017 Biomedical Science Tower 3, 3501 Fifth Avenue, Pittsburgh, PA 15261
Email: thanos@pitt.edu

Abstract

Peripheral damage drives auditory cortex (ACtx) plasticity, but the underlying synaptic and cellular mechanisms remain poorly understood. We used a combination of *in vitro* slice electrophysiology, optogenetics, and *in vivo* two-photon imaging to investigate layer 5 extratelencephalic (ET) and layer 6 corticothalamic (CT) neuronal plasticity in mice, following noise-induced hearing loss (NIHL). Thalamocortical (TC) input was initially balanced between CTs and ETs but shifted to CT-dominant one day post-NIHL and then normalized by day seven. This transient shift was accompanied by increased quantal size and suprathreshold excitability in CTs, with minimal changes in ETs. *In vivo*, CTs exhibited persistent elevation in sound intensity thresholds, while ETs showed a transient shift in frequency tuning and reduced high-frequency responsiveness that recovered within a week. These findings reveal distinct, cell-type-specific plasticity mechanisms in deep-layer ACtx neurons following peripheral damage and highlight potential targets for treating hearing loss-related disorders such as tinnitus and hyperacusis.

Keywords

auditory cortex, noise-induced hearing loss, plasticity, thalamocortical circuits, excitatory neurons, in vivo imaging, in vitro electrophysiology

Introduction

In all sensory systems, damage to peripheral organs induces compensatory plasticity mechanisms in the brain, which contributes to preserving function by increasing neural responsiveness to surviving sensory inputs. In the cortex, this homeostatic plasticity is characterized by increased central gain and has been well documented across sensory modalities (Rasmusson, 1982; Merzenich et al., 1983; Robertson and Irvine, 1989; Kaas et al., 1990; Gilbert and Wiesel, 1992). In the auditory system, exposure to loud noise induces cochlear damage that often leads to a reduction in auditory nerve input due to cochlear synaptopathy and the degeneration or death of both hair and spiral ganglion cells (Ryan and Bone, 1978; Liberman and Dodds, 1984; Kujawa and Liberman, 2009). Despite this peripheral damage, the sound-evoked activity of excitatory cortical principal neurons is frequently restored, or even enhanced, within days of noise-induced hearing loss (NIHL; (Qiu et al., 2000; Auerbach et al., 2014; Chambers et al., 2016; Resnik and Polley, 2017; Kumar et al.), reflecting robust cortical and subcortical homeostatic plasticity mechanisms. These mechanisms support perceptual hearing threshold recovery, especially in quiet backgrounds, even after a dramatic loss of peripheral input (Chambers et al., 2016; Resnik and Polley, 2021)

In the auditory cortex (ACtx), noise-induced cochlear damage is associated with enhanced central gain, reduced cortical inhibitory (GABAergic) activity, increased spontaneous firing, and reorganization of frequency tuning towards less damaged regions of the cochlea (Seki and Eggermont, 2003; Kotak et al., 2005; Sarro et al., 2008; Scholl and Wehr, 2008; Yang et al., 2011; Takesian et al., 2013; Chambers et al., 2016; Resnik and Polley, 2017). Recent studies in ACtx layer (L) 2/3 neurons revealed that this plasticity is mediated by cell-type-specific mechanisms, enabling a precise and cooperative division of labor amongst cortical interneurons (Kumar et al., 2023). However, the plasticity mechanisms governing excitatory projection neurons remain less understood. Addressing this knowledge gap requires examining the distinct contributions of deep-layer neurons, specifically L5 extratelencephalic neurons (ETs, also known as pyramidal tract or PT neurons) and L6 corticothalamic neurons (CTs), as L5 and 6 represent the primary output pathways from the ACtx. CTs exclusively target the thalamus and readily modulate local cortical gain, while also modulating ongoing thalamocortical oscillatory activity, forming key nodes in cortico-thalamo-cortical loops (Olsen et al., 2012; Guo et al., 2017; Ibrahim et al., 2021; Shepherd and Yamawaki, 2021). ETs also project to the thalamus as well as the midbrain, striatum, and amygdala (Harris and Shepherd, 2015; Chen et al., 2019; Williamson and Polley, 2019; Shepherd and Yamawaki, 2021; Issa et al., 2023). These projections are crucial for connecting the auditory system to downstream targets involved in motor control, sensorimotor integration, learning, and higher-order cognitive processes (Winer, 2005; Bajo et al., 2010; Stebbings et al., 2014; Xiong et al., 2015; Ford et al., 2024; Quass et al., 2024). It is therefore essential to determine how ETs, CTs, and their thalamocortical inputs change after NIHL. Given the importance of cortico-thalamo-cortical loops in perception and cognition in normal and pathological states (Tononi and Edelman, 1998; Tononi et al., 1998; Jones, 2001; Llinas et al., 2005; Sherman, 2007; Shepherd and Yamawaki, 2021), understanding these mechanisms may highlight novel approaches to enhance perceptual recovery after hearing loss and mitigate plasticity-induced disorders such as tinnitus and hyperacusis (Henton and Tzounopoulos, 2021).

To address these gaps in knowledge, we employed a mouse model of NIHL to investigate plasticity mechanisms after noise trauma. We used a combination of *in vitro* slice electrophysiology and *in vivo* two-photon imaging to characterize changes in thalamocortical synaptic strength, intrinsic excitability, and sound response properties of ETs and CTs after NIHL. Our findings highlight cell-type-specific plasticity mechanisms, offering insights into cortical plasticity in response to peripheral damage.

Materials and Methods

Animals

All mice handling was approved by the Institutional Animal Care and Use Committee at the University of Pittsburgh. 66 male and 38 female Ntsr1-Cre mice (MMRRC, B6.FVB(Cg)-Tg(Ntsr1-Cre)GN220Gsat/Mmcd) were used for experiments shown in Figures 1-5, S1-2; 3 male and 1 female Ntsr1-Cre mice as well as 4 male and 5 female Ntsr1-Cre x Ai148 mice (JAX, Ai148(TIT2L-GC6f-ICL-tTA2)-D) were used for Figure 6; 7 male and 2 female C57Bl/6J mice were used for Figure 7.

Surgical methods for *in vitro* electrophysiology

Mice (P28-35) were anesthetized with isoflurane (induction: 3% in oxygen, maintenance: 1.5-2% in oxygen) and secured in a stereotaxic frame (Kopf). Core body temperature was maintained at ~37°C with a heating pad and eyes were protected with ophthalmic ointment. Lidocaine (1%) was injected under the scalp and a midline incision was made to expose the skull. ETs were retrogradely labeled by injecting green fluorescent latex microspheres (Lumafluor) into the right inferior colliculus (1 mm posterior to lambda and 1 mm lateral, at an injection depth of 0.75 mm), schematized in **Figure 1A**. To transduce CTs, an AAV (AAV9-FLEX-tdTomato, titer: $1e^{13}$ gc/mL, 1:2 dilution in PBS, Addgene) was injected into the right ACtx of Ntsr1-Cre mice through a small burr hole (~0.4 mm diameter, ~4 mm lateral to lambda). A glass micropipette containing the viral vector was lowered into ACtx to a depth of ~1 mm using a micromanipulator (Kopf). A syringe pump (World Precision Instruments) was then used to inject 200 nL over the course of 2 minutes, at a rate of 100 nL/min.

To facilitate stimulation of thalamic afferents, 500 nL of AAV9-CaMKIIa-hChR2(H134R)-EYFP (titer: $8.96e^{13}$ gc/ml, Addgene) was injected into the right medial geniculate body (MGB) of Ntsr1-Cre mice (3 mm posterior/2 mm lateral/3 mm deep) at a rate of 100 nL/min, alongside injections of microspheres and AAV9-FLEX-tdTomato, as described earlier. This resulted in widespread expression across multiple MGB subdivisions. Post injection, the scalp was closed with cyanoacrylate adhesive and mice were given a subcutaneous injection of carprofen (5 mg/kg).

Surgical methods for *in vivo* two-photon imaging

Mice (P56-72) were anesthetized with isoflurane (induction: 5% in oxygen, maintenance: 1.5-2% in oxygen) and secured in a stereotaxic frame (Kopf). Dexamethasone (2 mg/kg) was administered via an intraperitoneal injection to mitigate brain edema. Core body temperature was maintained at ~37 °C with a heating pad and eyes were protected with ophthalmic ointment. Lidocaine (1%) was injected under the scalp and a midline incision was made to expose the skull. To transduce ETs, an AAV (AAVretro-hSyn1-GCaMP6s-P2A-nls-tdTomato, titer: $5e^{12}$ gc/mL, Addgene), was injected into the right inferior colliculus of C57 mice through a small burr hole (5 mm posterior to bregma and 1.2 mm lateral). A glass micropipette containing the viral vector was lowered to depths of 0.3 and 0.8 mm using a micromanipulator (Kopf). A syringe pump (Nanoject III, Drummond) was used to inject 300 nL at each site at a rate of 10-15 nL/min. CTs were transduced with GCaMP6s through intracranial injection into the ACtx (AAV5-Syn-FLEX-GCaMP6s-WPRE-SV40, titer: $7e^{12}$ gc/mL, Addgene) or through transgenic crossing with the Ai148 mouse line. Post injection, the scalp was closed with nylon sutures and mice were administered with a subcutaneous injection of carprofen (5 mg/kg). Viruses were allowed to express for a minimum of three weeks prior to two-photon imaging. Cranial windows were created by stacking three round glass coverslips (one 4 mm, two 3 mm, #1 thickness, Warner Instruments), etched with piranha solution (sulfuric acid and hydrogen peroxide), then glued together with optically transparent, UV-cured adhesive (Norland Products). The skull was exposed by removing the dorsal portion of the scalp and periosteum, then treated with etchant (C&B metabond) followed by 70% ethanol. A custom stainless steel headplate (iMaterialize,

(Romero et al., 2020) was then attached to the skull using dental cement (C&B metabond). A 3 mm circular craniotomy was made over right ACtx and the cranial window was placed into the opening. An airtight seal was achieved using Kwik-Sil (World Precision Instruments) around the edge of the window before cementing it into place. Vetbond (3M) was used to bind the surrounding tissue to the dental cement. Following the implant surgery, mice were given a subcutaneous injection of carprofen (5 mg/kg). Implants were allowed to heal for at least five days before the first day of imaging.

Slice electrophysiology

Mice (P58-65) were first anesthetized with isoflurane and then immediately decapitated. Brains were rapidly removed and coronal slices (300 µm) containing right ACtx were prepared in a cutting solution at 1 ^{o}C using a Vibratome (VT1200 S, Leica). The cutting solution (pH 7.4, ~300 mOsm) contained (in mM): 2.5 KCl, 1.25 NaH_2PO_4, 25 $NaHCO_3$, 0.5 $CaCl_2$, 7 $MgCl_2$, 7 Glucose, 205 sucrose, 1.3 ascorbic acid, and 3 sodium pyruvate (bubbled with 95% O_2/5% CO_2). Slices were immediately transferred to a holding chamber and incubated at 34 °C for 40 min before recording. The holding chamber contained ACSF, with the following composition (in mM): 125 NaCl, 2.5 KCl, 26.25 $NaHCO_3$, 2 $CaCl_2$, 1 $MgCl_2$, 10 glucose, 1.3 ascorbic acid, and 3 sodium pyruvate, pH 7.4, ~300 mOsm (bubbled with 95% O_2/5% CO_2). After incubation, slices were stored at room temperature until recording.

Whole-cell recordings in voltage- and current-clamp modes were performed in slices bathed in 31 ^{o}C carbogenated ACSF, identical to the incubating solution. Borosilicate pipettes (World Precision Instruments) were pulled into patch electrodes with 3–6 MΩ resistance (Sutter Instruments). For current-clamp recordings, pipettes were filled with a potassium-based intracellular solution, containing (in mM): 128 K-gluconate, 10 HEPES, 4 $MgCl_2$, 4 Na_2ATP, 0.3 Tris-GTP, 10 Tris phosphocreatine, 1 EGTA, and 3 sodium ascorbate (pH = 7.25, 295 mOsm). For voltage-clamp recordings of optogenetically-evoked excitatory postsynaptic currents (EPSCs), a cesium-based internal solution was used, containing (in mM): 126 $CsCH_3O_3S$, 4 $MgCl_2$ 10 HEPES, 4 Na_2ATP, 0.3 TrisGTP, 10 Tris-phosphocreatine, 1 CsEGTA, 1 QX-314, and 3 sodium ascorbate (pH = 7.25, 295 mOsm). Recordings were made using a MultiClamp-700B amplifier with a Digidata-1440A A/D converter and Clampex software (Molecular Devices). Data were sampled at 10 kHz and filtered at 4 kHz. Pipette capacitance was compensated, and series resistance (R_{series}) was maintained below 25 MΩ. R_{series} was measure in voltage clamp mode (command potential set at -70 mV) by applying a -5 mV voltage step and calculating the ratio of the step voltage to the peak current immediately following the step. Input resistance (R_{input}) was calculated in voltage-clamp mode (command potential set to -70 mV) by giving a -5 mV step, which resulted in transient current responses. The difference between baseline and steady state hyperpolarized current (ΔI) was used to calculate R_{input} using the following formula: $R_{input} = -5\ mV/\Delta I - R_{series}$. Resting membrane potential (V_{Rest}) was measured in current-clamp mode (I = 0) by averaging membrane potential for 20 sec after break-in. For intrinsic property measurements, the following drugs were included in the bath: 20 µM DNQX (AMPA receptor antagonist), 50 µM APV (NMDA receptor antagonist), and 20 µM SR 95531 Hydrobromide (Gabazine - a $GABA_A$ receptor antagonist). Depolarizing current pulses (25 pA increments of 1 sec duration) were injected from a holding potential of -70 mV (adjusted with DC current if necessary) to assess suprathreshold firing properties. Action potential (AP) width was defined as the full width at the half-maximum amplitude of the first AP at rheobase. AP threshold was determined from the phase-plane plot as the membrane potential where the depolarization slope (dV/dt) exceeded 10 V/sec.

Light-evoked EPSCs and strontium quantal events (Sr^{2+}-mEPSCs) were evoked by optogenetic stimulation of presynaptic axons. A collimated blue LED light source (470 nm, Thorlabs) was directed through a diaphragm and a 40x microscope objective lens, restricting illumination to a

small spot within the targeted cortical layer. ETs and CTs were selected for dual whole-cell recordings based on visual alignment along the radial (depth) axis using differential interference contrast optics. To ensure anatomical proximity consistent with columnar organization, we assessed the tangential (horizontal) distance between the somata of the recorded pairs. Post-hoc measurements across all recorded pairs revealed that the mean tangential distance was approximately 20 µm (18.81 ± 1.86 µm; n = 59 pairs). The light intensity required to elicit a stable, maximal plateau response was determined for each cell pair using a 0.15 ms light pulse. EPSCs were recorded in voltage clamp mode at -70 mV. Peak amplitudes were averaged over a 1 ms window. To isolate monosynaptic responses, recordings were performed in the presence of tetrodotoxin (TTX, 1µM) to block sodium channels and 4-aminopyridine (4-AP, 100 µM) potassium channel blocker to depolarize the terminals. Representative traces for figures were generated by averaging 10 consecutive EPSCs.

Sr^{2+}-mEPSCs were recorded in slices incubated for 30 mins in a modified Sr^{2+}-ACSF solution containing (in mM): 125 NaCl, 2.5 KCl, 26 $NaHCO_3$, 4 $SrCl_2$, 4 $MgCl_2$, 15 glucose, 1.3 ascorbic acid, and 3 sodium pyruvate, pH 7.4, ~300 mOsm, oxygenated w/ 95% O_2-5% CO_2. All other recording conditions, including the cutting solution, cesium-based internal solution, and light stimulation, remained the same as described above. Data were analyzed using Clampfit (11.2). A 400 ms window preceding LED onset (pre-LED) and a 400 ms window beginning 100 ms after LED onset (post-LED) were used for event detection. The amplitude of LED-evoked quantal events was calculated using the equation: $\frac{[(Apost*Fpost)-(Apre*Fpre)]}{Fpost-Fpre}$, where $Apost$ is the average amplitude of post-LED Sr^{2+}-mEPSCs, $Fpost$ is the frequency of post-LED events, $Apre$ is the average amplitude of pre-LED events, and $Fpre$ is their frequency (Whitt et al., 2022). Event detection was optimized by lowpass filtering the traces with a 1 kHz Gaussian filter. Events were included if they had a rise time < 3 ms and amplitude > 3 x root mean square (RMS) noise. Cells with RMS noise > 2 or where $Fpost$ - $Fpre$ < 2 Hz were excluded from the analysis.

Noise and sham exposure

23-29 days after viral injections, mice were anesthetized with isoflurane (induction: 3% in oxygen, maintenance: 1.5-2% in oxygen) during a unilateral noise exposure procedure. A plastic pipette tip, connected to a calibrated speaker (FT17H, Fostex), was inserted into the left ear. Core body temperature was maintained at ~37 °C with a heating pad and eyes were protected with ophthalmic ointment. Sham- and noise-exposed mice were treated identically, but noise-exposed mice were presented with 8-16 kHz broadband noise at 116 dB SPL for one hour.

Bandwidth limiting was achieved using a DS360 Ultra-Low Distortion Function Generator (Stanford Research Systems) in combination with a 3-pole Butterworth filter. The speaker (Type 4231, Brüel & Kjær) was calibrated using a 1/4-inch microphone (Model 4954-B, Brüel & Kjær) to accurately determine the output voltage required to achieve the desired sound level.

Auditory brainstem responses (ABRs)

ABR measurements were made from the left (exposed) ear and conducted in a sound-attenuating chamber (ENV-022SD, Med Associates). Subdermal electrodes were positioned with the active electrode at the vertex, the ground electrode ventral to the right pinna, and the reference electrode ventral to the left pinna. A calibrated speaker (CF-1, Tucker-Davis Technologies) delivered acoustic stimuli to the left ear via a pipette tip affixed to a plastic tube connected to the speaker. ABR measurements were recorded in response to 1 ms tone bursts at 10, 16, 24, and 32 kHz, presented in descending order from 80 to 0 dB SPL (or until 10 dB SPL below threshold). Threshold was defined as the lowest stimulus intensity that evoked a detectable Wave 1 response. A Wave 1 response was identified as the first consistent deflection that decreased in

amplitude and increased in latency as sound intensity decreased, distinguishing it from background noise. ABR measurements were acquired using BioSigRX software at a rate of 18.56 Hz, averaged over 512 repetitions, and filtered with a 300-3,000 Hz bandpass filter.

Two-photon imaging

Mice (P55-104) were acclimated to head fixation in the two-photon imaging rig for 30 min/day for three consecutive days before the start of experiments. Imaging was performed at three timepoints: one day pre-exposure (-1d), one day post-exposure (1d), and seven days post-exposure (7d). No additional head-fixation occurred between 1d and 7d. ABRs were performed before each imaging session to assess peripheral sound responses and hearing status. Mice with ABR click thresholds of 50 dB SPL or greater on -1d were excluded from the study. Noise-exposed mice were excluded if their click thresholds increased by less than 10 dB SPL from -1d to 1d. Similarly, sham-exposed mice were excluded if their click thresholds increased by more than 10 dB SPL across the same timepoints.

On -1d, widefield epifluorescence imaging was used to generate an ACtx tonotopic map, allowing identification of primary auditory area A1 (Romero et al., 2020). The two-photon field of view (FoV) was centered over A1 for all subsequent recordings. Two-photon excitation was provided by an Insight X3 laser tuned to 940 nm (Spectra-Physics). A 16x/0.8NA water-immersion objective (Nikon) was used to obtain a 512 x 512 pixel FoV at 30 Hz with a Bergamo II Galvo-Resonant 8 kHz scanning microscope (Thorlabs). Scanning software (Thorlabs) and stimulus generation hardware (National Instruments) were synchronized with digital pulse trains. For both widefield and two-photon imaging, the microscope was rotated 40-55 degrees from the vertical axis to image the lateral portion of mouse ACtx while the mouse remained upright. Imaging was conducted in a dark, sound attenuating chamber, and mice were monitored using infrared cameras (Genie Nano, Teledyne).

ETs were imaged 420-580 μm below the pial surface using laser powers of 45-130 mW, while CTs were imaged 600-790 μm below the pial surface with powers ranging from 111-150 mW. Fluorescence images were acquired at either 1x (750 x 750 μm) or 2x (375 x 375 μm) digital zoom. Raw calcium imaging data were processed using Suite2P (Pachitariu M, 2016) to perform rigid/non-rigid registration, region of interest (ROI) detection, and spike deconvolution. All ROIs were visually curated, and any low quality or non-somatic ROIs were excluded from further analysis. The same FoV was imaged across all three timepoints. Individual neurons were matched across days using ROIMatchPub, an open-source MATLAB plugin (https://github.com/ransona/ROIMatchPub).

Each imaging session included the presentation of two stimulus sets. Eight pure tones (4 - 45 kHz in half-octave steps) were presented at four intensities (20 - 80 dB SPL in 20 dB SPL steps). In addition, white noise bursts were presented at seven intensities (20 - 80 dB SPL in 10 dB SPL steps). All stimuli were 50 ms in duration, followed by a 2 sec inter-trial interval. Stimuli were delivered in a pseudorandom order, and each stimulus was repeated 20 times.

Two-photon imaging analysis

Deconvolved calcium traces (**Figure S3A**) were normalized for each cell by z-scoring relative to the average baseline activity during the 500 ms preceding sound onset. Evoked stimulus responses were quantified as the mean z-scored activity during the 0 - 500 ms window following sound onset. To determine whether a neuron was responsive to the given stimulus, the z-scored activity during the stimulus window was compared to 1000 samples of time-shifted responses, generated by circularly shifting the trace by 5 - 20 sec. A neuron was considered significantly responsive if its evoked response exceeded the 98th percentile of the randomly shifted distribution

(adapted from Khoury et al 2023). The best frequency of each neuron was defined as the frequency that evoked the highest z-scored response after averaging across intensities. Intensity thresholds were defined as the lowest sound intensity that produced a significant z-scored response.

Stimulus decoding

We trained a multinomial logistic regression classifier to decode stimulus identity (either pure tone frequency at 80 dB SPL or white noise intensity) on a trial-by-trial basis. All neurons were pooled across mice for each exposure and day condition. Using 5-fold cross-validation, the classifier was trained on the mean evoked activity (0 - 500 ms following sound onset) from 200 randomly-selected neurons. Decoding accuracy was quantified as the fraction of correctly classified trials in the held-out test set. Because the full dataset contained between 562 to 2687 neurons per condition, we repeated this decoding procedure 2000 times, each time resampling (with replacement) a new population of 200 neurons. This resampling strategy ensures that decoding accuracy estimates were not biased by group size differences. We then calculated the mean and standard deviation of the resultant decoding accuracy distribution for each exposure/day condition. P values were computed explicitly from the bootstrapped distributions of decoding accuracies (Day and Delgutte, 2016).

Image processing

Image captioning for Figure 1C was performed using Qcapture (QImaging). All images were imported and processed using ImageJ (https://imagej.nih.gov/ij/).

Statistics

For statistical comparisons between two independent groups that passed the Shapiro-Wilk test for normality, we used unpaired t-tests. For non-normally distributed data, Mann-Whitney U (rank-sum) tests were used. Comparisons involving more than two groups were assessed using N-way ANOVAs, with appropriate corrections for multiple comparisons. For correlation analyses, we calculated Spearman's rank correlation coefficient (rho). Significance levels are denoted as: *$P < 0.05$, **$P < 0.01$, ***$P < 0.001$, ****$P < 0.0001$. All group data are presented as mean ± SEM unless otherwise specified. See Tables 1 and 2 for detailed statistical values and test results.

Results

To induce a stereotyped hearing loss, we followed standard approaches (see Methods) and exposed mice to 8-16 kHz broadband noise at 116 dB SPL for 1 hour (noise-exposed, NE). As a control, a separate cohort of littermate mice was sham-exposed (SE) using identical procedures, but without noise presentation. To assess hearing thresholds pre and post NE or SE (-1d, 1d, and 7d), we measured auditory brainstem responses (ABRs) (**Figure S1A-H**), which reflect the synchronous activity of auditory nuclei, from the auditory nerve (wave I) to the inferior colliculus (wave V) (**Figure S1I**). Following NE, we observed significantly elevated ABR thresholds and reduced wave I amplitudes both 1d (**Figure S1A-I**) and 7d (**Figure S2A-H**) after NE, across all tested frequencies. In contrast, ABR thresholds and wave I amplitudes were unchanged in SE mice (**Figure S1A-I**). Together, these data confirm that our NE protocol produces a persistent hearing threshold shift lasting at least one week.

Transient shift in TC synaptic strength from CT and ET equivalent to CT dominant one day after NE

Communication between ACtx and the auditory thalamus, the MGB, is mediated by reciprocally connected corticothalamic (CT) and thalamocortical (TC) pathways. TC neurons in the MGB provide strong input to ACtx, innervating both ETs and CTs (Hooks et al., 2013; Yamawaki and

Shepherd, 2015). However, the impact of NIHL on TC synaptic strength onto these two projection neuron populations remains unknown.

To address this question, we performed dual recordings from ETs and CTs within the same brain slice while photoactivating TC axons. This recording configuration enabled us to calculate the ratio of synaptic strength at TC→CT versus TC→ET synapses (the CT/ET ratio) under identical experimental conditions. Although comparing absolute EPSC amplitudes with optogenetic recordings is not ideal due to variability in viral infection efficiency per mouse/brain area, the dual recording approach of the CT/ET ratio is well-suited for detecting relative, noise-induced changes in TC input strength between CTs and ETs.

To study TC→CT and TC→ET synapses, we drove expression of channelrhodopsin-2 (ChR2) in CAMKII-expressing MGB neurons by injecting AAV-CaMKII-ChR2-YFP into the MGB (**Figure 1A-C,** see Methods). To stimulate ChR2-expressing TC axons, we used a collimated blue LED light source directed through a diaphragm and a 40x microscope objective lens. Monosynaptic photo-evoked AMPA receptor (AMPAR)-mediated EPSCs were recorded simultaneously from vertically aligned ETs (green) and CTs (red) (**Figure 1A-C**). To selectively label ETs and delineate ACtx boundaries, we injected green fluorescent microspheres (retrobeads) into the right inferior colliculus (IC, **Figure 1A, and 1C, middle**) (Joshi et al., 2015; Joshi et al., 2016). To selectively label CTs, we injected Ntsr1-Cre transgenic mice, which selectively express Cre-recombinase in CTs, with AAV-FLEX-tdTomato (**Figure 1C, right**). All electrophysiological experiments were performed in the presence of TTX to block action potentials, and 4-AP to enhance presynaptic depolarization (see Methods). Because CT dendrites are primarily restricted to the deep cortical layers, photostimulation was confined to L5-6 (**Figure 1B**).

One day after NE, we observed a dramatic shift in TC input from equivalent (CT/ET ratio ~ 1) to CT dominant (CT/ET ratio > 5) (two-way ANOVA, main effect for exposure, $F = 5.44$, $p = 0.02$; main effect for day, $F = 2.25$, $p = 0.14$). By 7d post-exposure, TC input had recovered to a balanced state, with equivalent excitation of CTs and ETs (**Figure 1D, F**). Together, these results indicate that NIHL transiently enhances thalamic excitation of CTs relative to ETs, which recovers 7d after NE.

Transient increase in the *q* on TC→CT synapses 1 day after NE

To understand the mechanisms underlying the shift toward greater relative thalamic excitation of CTs relative to ETs, we next examined the synaptic properties of TC→CT and TC→ET synapses, as well as the intrinsic excitability of CTs and ETs following NE. Because these recordings were performed in the presence of TTX and 4-AP, and the ChR2 activation directly depolarized presynaptic terminals, the probability of release (p) was likely saturated at all synapses (n). We therefore chose to assess the quantal size (q), first, in TC→CT synapses.

To evaluate the amplitude of quantal events, we replaced calcium (Ca^{2+}) with strontium (Sr^{2+}) in the bath solution (**Figure 2A-D**). Sr^{2+} desynchronizes evoked neurotransmitter release, allowing the analysis of quantal events originating from the stimulated synapses (**Figure 2A-D**) (Oliet et al., 1996; Kouvaros et al., 2020). Following maximal photostimulation of L5-6, we observed a significant increase in the average amplitude of quantal events at TC→CT synapses 1d after NE (unpaired t-test, $p = 0.04$; **Figure 2A-B**), which recovered by 7d after NE (unpaired t-test, $p = 0.68$; **Figure 2C-D**). This increase in q likely reflects enhanced synaptic strength at TC→CT synapses, either due to postsynaptic changes or changes in vesicle content. Consistent with these findings, we also found that average TC→CT EPSC amplitudes, elicited by L5-6 photostimulation, were significantly enhanced 1d after NE compared to SE (Mann-Whitney U test,

p = 0.004; **Figure 2E-F**), which then recovered by 7d (unpaired t-test, p = 0.94; **Figure 2G-H**). Together, these results suggest that an increase in *q* at TC→CT synapses contribute to the greater relative thalamic excitation in TC→CT compared to TC→ET after NE.

Transient increase in CT suprathreshold intrinsic excitability one day after NE

Next, we investigated the effect of NE on CT intrinsic excitability. Neither input resistance (R_{input}) nor action potential width or threshold (AP_{width}, AP_{thres}) changed at either 1d or 7d after NE (**Figure 3A, C-D**). However, the resting membrane potential (V_{rest}) was significantly more hyperpolarized 1d after NE (two-way ANOVA, main effect for exposure, F = 19.81, p < 0.0001; main effect for day, F = 9.40, p = 0.003; exposure x day interaction, F = 6.91, p = 0.01; **Figure 3B**). We also observed a significant difference in the V_{rest} of SE mice between 1d and 7d (two-way ANOVA, Bonferroni corrected for multiple comparisons, p = 0.0007). However, this difference does not impact the main conclusions of the study, which are based on comparisons between well-controlled SE and NE groups. When we evaluated suprathreshold excitability, we found that CTs displayed a significant increase in overall firing frequency in response to depolarization (two-way ANOVA, main effect for exposure, F = 9.45, p = 0.004; exposure x current steps interaction, F = 3.82, p < 0.0001; **Figure 3E-F**), suggesting an increased suprathreshold excitability of CTs concurrent with increased TC→CT input 1d after NE. There were no differences in CT intrinsic suprathreshold excitability between SE and NE mice 7d after exposure (two-way ANOVA, main effect for exposure, F = 2.64, p = 0.11; exposure x current steps interaction, F = 0.91, p = 0.52; **Figures 3G-H**). Taken together, these results suggest that despite a transient hyperpolarization of V_{rest} after NE, a combination of intrinsic and synaptic mechanisms that increase TC→CT synaptic strength and CT suprathreshold excitability likely contribute to the shift of TC input from equivalent between CT and ET to CT dominant 1d after NE.

No changes in the *q* of TC→ET synapses after NE

We next assessed TC→ET synapses using a similar electrophysiological approach as described for TC→CT synapses (**Figure 2)**. We found no significant changes in *q* at either 1d or 7d following NE (1d, Mann-Whitney U test, p = 0.64; 7d, Mann-Whitney U test, p > 0.9999; **Figure 4A-D**). However, the average TC→ET EPSC amplitudes were significantly reduced 1d after NE compared to SE (two-way ANOVA, main effect for exposure, F = 8.32, p = 0.005; main effect for day, F = 0.05, p = 0.82; exposure x day interaction, F = 4.97, p = 0.03; **Figure 4E-F**). This reduction was recovered by 7d post NE (**Figure 4E,F**). Given that *p* is likely saturated in TC→ET synapses, and *q* remained unchanged, the reduction in L5-6 TC→ET EPSCs likely reflects a decrease in *n*. Alternatively, this result may be influenced by the inherent limitations of our experimental setup, particularly variability in AAV infection efficiency across mice and brain areas, which can complicate interpretation of synaptic strength (see Discussion).

Because ETs have extensive dendritic arbors throughout the cortical column, and TC projections to ETs span several cortical layers (Harris and Shepherd, 2015; Ji et al., 2016), we also evaluated TC→ET EPSCs elicited after photostimulating L1-4 (L1-4 TC EPSCs) . No significant differences were observed at either 1d or 7d after NE (two-way ANOVA, main effect for exposure, F = 1.88, p = 0.18; main effect for day, F = 1.43, p = 0.24; exposure x day interaction, F = 3.35, p = 0.08; **Figure 4G-H**). Together, these findings support a cell-type-specific increase in *q* at TC→CT synapses, which likely contributes to the enhanced thalamic excitation onto CTs relative to ETs 1d after NE. Additionally, our results suggest that the observed increase in the CT/ET ratio is likely influenced by the reduction in TC→ET EPSC amplitude **(Figure 4E)**, although the absolute magnitude of this decrease should be interpreted with caution due to the limitations of our optogenetic stimulation approach (see Discussion).

446
447 **No changes in ET intrinsic excitability after NE**
448 After establishing that NIHL differentially affects TC input onto ETs versus CTs, we next examined
449 whether NE also alters the intrinsic excitability of these neurons in a cell-type-specific manner.
450 R_{input}, V_{rest}, AP_{width}, $AP_{threshold}$, and firing frequency-current (F-I) functions were unchanged at both
451 1d and 7d post NE in ETs (**Figure 5A-H**). This finding supports cell-type-specific intrinsic plasticity
452 in deep layer neurons after NIHL, whereby ETs remain intrinsically stable while CTs exhibit a
453 transient decrease in subthreshold excitability and a transient increase in suprathreshold
454 excitability.
455
456 **Changes in CT sound response properties persist 7 days after NE**
457 To examine the consequences of NIHL in ET and CT sound response properties, we recorded
458 the sound-evoked activity of neural populations using two-photon (2P) calcium imaging. This
459 technique allowed us to longitudinally image the same populations of genetically defined cell-
460 types across time before and after noise exposure and characterize changes in sound response
461 properties. Head-fixed, awake mice passively listened to auditory stimuli, and we recorded
462 responses one day prior to exposure (-1d), then again one and seven days after exposure (1d
463 and 7d), matching our previous electrophysiological studies. We selectively expressed GCaMP6s
464 in CTs to examine how CT responses to sounds change following NE (**Figure 6A**, see Methods).
465 We imaged a total of 4943 CTs across 8 unique fields of view in SE mice (-1d: 1649 neurons; 1d:
466 1681 neurons; 7d: 1613 neurons) and 7731 CTs across 14 unique fields of view in NE mice (-1d:
467 2687 neurons; 1d: 2546 neurons; 7d: 2498 neurons). We then determined which neurons were
468 significantly active during sound presentation and used these sound-responsive neurons for all
469 subsequent analyses (see Methods).
470
471 We first examined frequency responses by presenting pure tones of varying frequencies (4-45
472 kHz in 0.5 octave steps) and intensities (20-80 dB SPL in 20 dB SPL steps; **Figure S3B**).
473 Averaging across intensity, we initially observed that CTs exhibited unstable frequency encoding,
474 as evidenced by fluctuations in average pure tone responses in SE animals (two-way ANOVA,
475 main effect for day, $F = 0.66$, $p = 0.52$; frequency × day interaction, $F = 3.68$, $p < 0.0001$; **Figure**
476 **6B**). Nevertheless, we observed strong changes in CT sound responses following NE (two-way
477 ANOVA, main effect for day, $F = 11.62$, $p < 0.0001$; frequency × day interaction, $F = 2.78$,
478 $p = 0.0004$; **Figure 6C**). CTs exhibited increased population responses to low frequency sounds
479 (4-11 kHz) 7 days after NE. Next, we compared average population tuning curves by aligning
480 activity to each neuron's best frequency (BF) and comparing these aligned tuning curves across
481 days. Frequency tuning curves remained stable in SE mice (two-way ANOVA, main effect for day,
482 $F = 0.52$, $p = 0.59$; frequency × day interaction, $F = 0.81$, $p = 0.67$; **Figure 6D**). NE induced a slight
483 but significant increase in responses 0.5 octaves below BF (two-way ANOVA, main effect for day,
484 $F = 9.36$, $p < 0.0001$; frequency × day interaction, $F = 0.52$, $p = 0.94$; **Figure 6E**). To investigate if
485 individual neurons altered their tuning preferences following noise exposure, we matched the
486 same cells across days and quantified changes in BF compared to baseline on day -1. While not
487 significant, CTs displayed a trend to decrease BF following NE (two-way ANOVA, main effect for
488 exposure, $F = 1.00$, $p = 0.32$; main effect for day, $F = 1.14$, $p = 0.32$; frequency × day interaction,
489 $F = 1.33$, $p = 0.27$; **Figure 6F**). To examine how these changes in frequency responses impacted
490 population encoding, we used a multinomial logistic regression model to predict stimulus
491 frequency from neural activity. Decoding frequency identity from CT activity did not reveal any
492 effect of noise exposure on population-level encoding (**Figure 6G**). Together, these results
493 suggest that noise exposure does not profoundly change CT frequency tuning.
494
495 We next examined intensity tuning by presenting broadband noise bursts between 20-80 dB SPL
496 (in 10 dB SPL steps). As with pure tone responses, CTs showed subtle changes in broadband

noise responses following SE (two-way ANOVA, main effect for day, $F = 3.54$, $p = 0.03$; frequency × day interaction, $F = 2.51$, $p = 0.003$; **Figure 6H**). In contrast, there was a marked decrease in intensity responses following NE (two-way ANOVA, main effect for day, $F = 13.87$, $p < 0.0001$; frequency × day interaction, $F = 5.45$, $p < 0.0001$; **Figure 6I**). Specifically, CTs exhibited decreased activity in response to low intensity noise (< 60 dB SPL) following NE, which did not recover by 7d. There was also a slight but significant increase in responses to 80 dB SPL noise 7d after NE. Consequently, NE led to a significant increase in intensity thresholds (two-way ANOVA, main effect for exposure, $F = 14.75$, $p = 0.0002$; main effect for day, $F = 4.165$, $p = 0.02$; frequency × day interaction, $F = 4.94$, $p = 0.008$; **Figure 6J**). This was also evident when looking at the absolute intensity thresholds (**Figure S4A**). Despite these changes, decoding analyses did not reveal any significant changes in population encoding (**Figure 6K**). Together, this suggests that noise exposure leads to decreased sensitivity in CTs to low intensity noise that does not recover within a week.

Transient changes in ET sound response properties 1 day after NE

We next examined the activity of ETs through selective expression of GCaMP6s (**Figure 7A**, see Methods). We imaged a total of 2337 ETs across 9 unique fields of view in 5 SE mice (-1d: 705 neurons; 1d: 820 neurons; 7d: 812 neurons) and 1703 ET neurons across 8 unique fields of view in 4 NE mice (-1d: 562 neurons; 1d: 565 neurons; 7d: 576 neurons). As before, only neurons that were significantly active during sound presentation were used for subsequent analyses.

We found that the average population responses to pure tones remained unchanged in SE mice (two-way analysis of variance (ANOVA), main effect for day, $F = 0.68$, $p = 0.51$; frequency × day interaction, $F = 1.03$, $p = 0.41$; **Figure 7B**). In contrast, NE led to a shift in the representation of frequencies across the ET population (two-way ANOVA, main effect for day, $F = 19.35$, $p < 0.0001$; frequency × day interaction, $F = 1.93$, $p = 0.02$; **Figure 7C**). 1d after NE, the average response to 23 kHz pure tones significantly decreased compared to baseline. This reduction in activity then recovered to baseline levels by 7d and was accompanied by a significant increase in response to lower frequency sounds (11-16 kHz). BF-aligned tuning curves were consistent across days in SE mice (two-way ANOVA, main effect for day, $F = 0.58$, $p = 0.56$; frequency × day interaction, $F = 0.58$, $p = 0.90$; **Figure 7D**). Conversely, NE led to significant changes in the average tuning curves (two-way ANOVA, main effect for day, $F = 12.03$, $p < 0.0001$; frequency × day interaction, $F = 1.84$, $p = 0.02$; **Figure 7E**). Specifically, 7d after NE, ETs increased the magnitude of their responses at, and one octave below, BF. This was accompanied by a significant decrease in BF itself on day 1 which then recovered by day 7 in NE animals (two-way ANOVA, main effect for exposure, $F = 17.67$, $p < 0.0001$; main effect for day, $F = 2.23$, $p = 0.11$; exposure × day interaction, $F = 11.34$, $p < 0.0001$; **Figure 7F**). Frequency decoding revealed that SE populations exhibited stable predictive accuracy across days, while NE led to a significant decrease in accuracy 1d after NE and a subsequent recovery 7d after NE (**Figure 7G**). These findings suggest that one day following NE, ETs reduce their activity at high frequencies and consequently shift to lower BFs, decreasing the ability to accurately decode stimuli from population activity. These perturbations then return to baseline seven days after NE.

We next examined whether ET intensity tuning changed following NE. As expected, noise responses were similar across days in SE mice (two-way ANOVA, main effect for day, $F = 0.20$, $p = 0.82$; intensity × day interaction, $F = 0.94$, $p = 0.50$; **Figure 7H**). We observed that NE led to significant changes in intensity responses (two-way ANOVA, main effect for day, $F = 8.01$, $p = 0.0003$; frequency × day interaction, $F = 2.90$, $p = 0.0005$; **Figure 7I**). 1d after NE, ETs displayed a loss of responses to low intensities (< 50 dB SPL) and a reduction in responses at higher intensities. On 7d, responses partially recovered but remained below baseline for 70 dB SPL. We then quantified changes in single neuron intensity thresholds with cells matched across imaging

days (two-way ANOVA, main effect for exposure, F = 11.23, p = 0.0009; main effect for day, F = 6.56, p = 0.002; exposure × day interaction, F = 3.496, p = 0.03; **Figure 7J**). 1d after NE, ETs displayed an increased threshold which reverted to baseline by 7d. This recovery was also evident when looking at the absolute intensity thresholds (**Figure S4D**). We also observed a threshold decrease 7d after SE, driven by a slightly higher threshold prior to exposure. Finally, we decoded sound intensity from population activity using multinomial logistic regression. Similar to our frequency decoding findings, we found that decoding accuracy transiently decreased 1d following NE (**Figure 7K**). Together, these findings suggest that ETs recover from transient changes in tuning to both frequency and intensity following noise exposure.

Changes in synaptic, intrinsic, and sound response properties correlate with hearing loss severity

To address whether the degree of neural plasticity was tied to the extent of hearing loss or recovery in individual animals, we correlated each animal's ABR click threshold shift with the magnitude of the synaptic, intrinsic, and sound response changes. We found that many of the measured plastic changes scaled significantly with trauma severity (**Figure 8**). In particular, the relative strengthening of TC input to CTs was more pronounced in animals with greater hearing loss: the CT/ET EPSC ratio was positively correlated with ABR threshold shift (**Figure 8A**; Spearman's ρ = 0.46, p = 0.002). The average L5-6 TC→CT *q* and EPSC amplitude increased with worsening ABR thresholds (**Figure 8B-C**; ρ = 0.34, p = 0.03), whereas TC→ET EPSCs were inversely related to hearing status (**Figure 8D**; ρ = –0.36, p = 0.02), further supporting both an enhanced synaptic TC drive onto CTs and a diminished TC drive onto ETs in mice with more severe hearing loss. In line with these synaptic effects, the intrinsic properties of CTs also covaried with hearing loss: animals with larger ABR threshold shifts had more hyperpolarized CT resting potentials (**Figure 8E**; ρ = –0.51, p = 0.002). We also noted that the increase in CT firing showed an overall positive trend with ABR shift (**Figure 8F**; max firing frequency; ρ = 0.31, p = 0.08), although this did not reach significance, likely due to the limited sample size for this measure, which is a general limitation for these correlations. Alternatively, this result could suggest that suprathreshold excitability changes occurred uniformly after trauma rather than scaling with severity of hearing loss.

We next asked whether the *in vivo* sound responses were related to the degree of hearing loss or recovery across animals. One day after exposure, the elevation in CT neuronal threshold (Δ intensity threshold) was positively correlated with ABR shift (**Figure 8G**; ρ = 0.32, p = 0.01). Animals with persistently high ABR thresholds retained larger CT threshold elevations 7d post exposure (**Figure 8H**; ρ = 0.31, p = 0.02). The transient threshold shift observed in ETs one day after exposure also scaled with hearing loss (**Figure 8I**; ρ = 0.23, p = 0.03). In contrast, ETs no longer showed a correlation by 7 days (**Figure 8J**; ρ = 0.07, p = 0.47), consistent with their response properties largely recovering despite the sustained peripheral deficit. Thus, inter-animal variability in both synaptic and sensory response plasticity generally tracked the severity of noise-induced hearing loss, whereas the rapid recovery of the ET projection by 7 days occurred regardless of residual hearing impairment.

Discussion

Our findings provide new insights into the cellular and circuit mechanisms underlying the cortical plasticity of deep-layer neurons in the auditory cortex (ACtx) following noise-induced hearing loss (NIHL). We identified distinct changes in the synaptic, intrinsic, and sound response properties of L5 extratelencephalic (ET) and L6 corticothalamic (CT) neurons. One day after NIHL, thalamocortical input was temporarily reweighted to favor CTs over ETs. We hypothesize that this transient shift in relative thalamic drive acts as a compensatory mechanism to preserve auditory signaling following peripheral damage. Overall, the cell-type-specific plasticity observed in ETs

and CTs advances our understanding of how ACtx adapts to cochlear injury and preserves hearing function post-NIHL.

Enhanced thalamocortical input and intrinsic excitability in L6 CT neurons after NIHL

CTs form reciprocal and nonreciprocal feedback loops with the thalamus to modulate TC activity through gain control and temporal filtering (Llano and Sherman, 2008; Olsen et al., 2012; Mease et al., 2014; Guo et al., 2017; Clayton et al., 2021; Ibrahim et al., 2021). Optogenetic experiments revealed a selective enhancement of TC input to CTs one day after NE. In simultaneous recordings of neighboring CTs and ETs, CTs received significantly stronger excitation from thalamic afferents compared to ETs one day after NE (**Figure 1**). Although our optogenetic approach could be influenced by variability in viral infection and a likely saturation of release probability under our recording conditions (**Figure 2E-H**, **Figure 4E-H**), the within-animal comparison between CTs and ETs effectively controls for the variability in viral infection. Importantly, quantal analysis, which permits comparison of synaptic strength across different animals and brain slices, also showed an increased quantal amplitude (*q*) at thalamocortical synapses onto CTs (**Figure 2A-D**), supporting a genuine upregulation of thalamocortical quantal synaptic strength onto CT circuits after noise trauma.

In parallel with these synaptic changes, CTs became intrinsically more excitable one day after NIHL, especially for suprathreshold stimuli (**Figure 3E-F**). The combination of enhanced synaptic excitation and intrinsic excitability suggests that CTs are poised to fire more readily in response to thalamic input following trauma. Such rapid strengthening of CT excitability likely represents an early homeostatic adjustment aimed at preserving cortical activity levels despite reduced cochlear input. Because CTs provide feedback to both the lemniscal (primary) and non-lemniscal auditory thalamus, their increased excitability could boost the overall gain of thalamocortical transmission and stabilize network activity across multiple circuits. This fast CT upregulation may be a compensatory mechanism to enhance perceptual processing after NIHL, potentially through improved sensory gain control and/or multisensory/contextual modulation (Jones, 1998, 2001; Super et al., 2001; Llinas et al., 2005; Larkum, 2013).

Persistent reduction in low-intensity sound responses of L6 CT neurons

Despite the overall increase in excitability of CTs, we observed a paradoxical reduction in their responsiveness to low intensity sounds following NIHL. One day after NIHL, CTs responded weakly to near-threshold tones, as shown by sound-evoked measurements *in vivo* (**Figure 6H-K**). This loss of sensitivity to faint sounds persisted one week after NIHL and cannot be explained by the enhanced thalamocortical input or intrinsic excitability described above (which would predict an increase in firing). One potential contributing factor is the slight hyperpolarization of CT V_{rest} observed one day after NIHL (**Figure 3B**), which could raise the spiking threshold. However, this intrinsic change is likely not the main cause, because by 7 days post-NIHL V_{rest} had returned to baseline, yet their low-intensity sound responses remained reduced. It is possible that changes in intracortical excitation or inhibition onto CTs may be selectively gating out weaker inputs after trauma. It is possible, for example, that CTs received enhanced feedforward inhibition or that their spike timing was altered *in vivo* in a way that requires a stronger synchronized input to elicit firing. Although we did not directly measure changes in L6 inhibitory circuits, any increase in local inhibition would further limit CT activity in response to weak stimuli, counterbalancing their higher intrinsic and thalamus-driven excitability.

Why might ACtx suppress responses to low intensity sounds after NIHL? One interpretation is that the auditory system is trading off raw sensitivity for reliability. By raising the threshold for ACtx responses to soft inputs, the system could avoid spurious firing to unreliable background noise. This idea is consistent with the notion that CT feedback circuits help resolve competing demands

of sound detection vs. discrimination (Olsen et al., 2012; Guo et al., 2017; Ibrahim et al., 2021). This nuanced plasticity in CTs, whereby global excitability increases but responsiveness to weak inputs decreases, potentially optimizes the signal-to-noise ratio of auditory cortical output after NIHL.

Minimal thalamocortical and intrinsic changes with transient retuning in L5 ET neurons after NIHL

In contrast to CTs, ETs exhibited relatively minimal changes in their intrinsic and synaptic properties after NIHL. We observed no significant alterations in ETs' intrinsic excitability at either 1 day or 7 days post-NIHL (**Figure 5**), consistent with previous studies (Nogueira et al., 2023).

While the quantal amplitude (*q*) of thalamocortical synapses onto ETs remained unaltered (**Figure 4A–D**), the most notable early synaptic effect on ETs was a transient reduction in overall thalamic drive observed one day post-NIHL (**Figure 4E–F**). Optogenetic EPSCs recorded from ETs were smaller at one day post-NIHL, which might indicate a decrease in the number of functional thalamic release sites (*n*), given the likely saturated probability of release during our recordings. We acknowledge that our optical stimulation approach has limitations (including variability in viral transduction and possible saturation of release probability), so the absolute magnitude of this reduction should be interpreted cautiously. Nevertheless, by 7 days post-NIHL the thalamocortical input to ETs had recovered (**Figure 4E, F**), and the balance of thalamic drive between CTs and ETs returned to near pre-NIHL levels. The early drop in ET input is thus best viewed as a short-term adjustment, likely contributing to the shift we saw toward CT-dominant thalamic excitation one day after noise trauma. Importantly, even at its weakest point, some thalamic input to ETs was preserved, allowing these neurons to continue participating in cortical processing during the acute phase after NIHL.

Although ETs showed little change in their excitability, they did undergo a rapid shift in sound-evoked tuning after NIHL. One day post-NIHL, ETs became less responsive to high-frequency tones (**Figure 7**). To compensate for this loss, ETs increased their gain 7d after NE. As a result, ETs recovered their frequency tuning (**Figure 7F**) but conversely responded proportionally more to lower-frequency inputs that were spared by the trauma (**Figure 7C,E**). Furthermore, ET population encoding largely returned to baseline (**Figure 7G,K**), coinciding with the recovery of thalamocortical input strength to ETs (**Figure 4E-F**). Such transient retuning and lasting gain enhancement likely helps the animal continue to perceive sounds in the frequency ranges that remain intact, thereby partially compensating for the loss at damaged frequencies.

Given the minimal intrinsic and postsynaptic changes in ETs, this reorganization is likely mediated by enhanced excitatory and/or decreased inhibitory intracortical inputs; however, our studies did not study these inputs. ETs are major sources of corticofugal projections to subcortical structures; thus, maintaining their sound-evoked activity may ensure continued engagement and/or trigger plasticity in downstream targets like the MGB and the inferior colliculus (IC) during the acute post-trauma period. This is supported by related findings that corticofugal outputs from L5 neurons become hyperactive after cochlear injury (Asokan et al., 2018). This sustained potentiation is thought to underlie network hyperexcitability and reorganization in the aftermath of hearing loss. Thus, the transient bias of ETs toward lower-frequency responsiveness in our study may reflect a functional routing of cortical drive to preserve auditory throughput to the thalamus and midbrain.

A caveat in our approach is that we identified ETs and CTs using different labeling strategies (retrobead tracing versus Cre-dependent viral tagging). Retrobeads remain sequestered in vesicles and are designed to be inert, causing minimal if any impact on neuronal health (Katz and Iarovici, 1990). Similarly, AAV labeling yields long-term fluorescent protein expression with low

toxicity and negligible effect on neuronal physiology at the doses used. Indeed, both approaches are widely used, often together, and are not known to alter intrinsic excitability or synaptic function (Joshi et al., 2015; Yamawaki and Shepherd, 2015; Joshi et al., 2016; Lur et al., 2016; Yamawaki et al., 2021; Kouvaros et al., 2023). Moreover, any subtle labeling-related effects (e.g., mild immune activation from viral infection) would be expected to affect sham- and noise-exposed groups equally and are therefore unlikely to confound the main conclusions of our study.

Layer-specific adaptive strategies in ACtx after NIHL

Our study of deep-layer ETs and CTs complements and extends recent research on plasticity in superficial layers of ACtx (Chambers et al., 2016; Resnik and Polley, 2017, 2021; Kumar et al., 2023), revealing a layer-specific pattern of adaptation after NIHL. Recent results showed that L2/3 interneurons exhibit cell-type-specific plastic changes following NIHL, with different subclasses of inhibitory neurons showing distinct time courses and levels of recovery (Resnik and Polley, 2021; Kumar et al., 2023) . Such findings underscore that each cortical layer (and cell-type) may deploy unique mechanisms to cope with degraded sensory input. In superficial layers, the priority may be maintaining local network stability and gain control. Adjustments in L2/3 circuits (especially among inhibitory interneurons) likely serve to enhance principal neuron gain while preventing hyperexcitability when thalamic input is reduced or imbalanced (Kumar et al., 2023). Although our study focused on plasticity in the deeper layers, we did not directly examine GABAergic interneuron changes. However, it is likely that the infragranular adaptations we observed are modulated by the alterations in inhibition occurring in supragranular layers. One potential mechanism is through cortical disinhibition: supragranular vasoactive intestinal peptide (VIP) interneurons, which become hyperactive post-trauma (Kumar et al., 2023), inhibit parvalbumin (PV) interneurons across layers (Letzkus et al., 2011; Pfeffer et al., 2013; Kullander and Topolnik, 2021), including those that normally target the apical dendrites of infragranular pyramidal cells. Thus, a reduction in PV activity after trauma would release deep-layer neurons from dendritic inhibition, allowing them to respond more strongly.

On the other hand, ETs and CTs engage in plasticity that appears geared toward preserving output and driving broader compensatory changes. These projection neurons are the main conduits of cortical influence on subcortical structures (ETs projecting to the thalamus, midbrain, and other sub-cortical centers, CTs projecting exclusively to the thalamus). The plastic changes in deep layers, such as enhanced CT excitability and transient ET retuning, suggest that deep-layer circuits are working to propagate adaptive signals throughout the auditory pathway and perhaps trigger plasticity in lemniscal, non-lemniscal, and even multisensory pathways. For instance, the rapid CT plasticity might initiate compensatory adjustments in thalamic relay neurons or even in other cortical areas by altering the feedback they provide to the MGB. Similarly, stable firing in ETs ensures that activity continues to flow to multiple subcortical centers, which could drive plastic reweighting or gain changes.

Complementary roles of ET and CT plasticity after NIHL

Viewed together, the divergent changes in ETs and CTs represent complementary adaptations that serve the shared goal of maintaining auditory function after NIHL. CTs, with their strengthened thalamic inputs and heightened intrinsic excitability, primarily contribute to normalizing cortical activity and refining sensory processing. By increasing the gain of thalamocortical transmission, CTs amplify the cortical representation of incoming sounds, which can compensate for reduced peripheral input. At the same time, our data suggest that CT circuits impose a stricter threshold for low-intensity inputs thereby filtering out noise and enhancing the discrimination of important signals. This dual action of CT plasticity (boosting overall responsiveness while gating insignificant inputs) aligns with models in which cortical feedback optimizes the trade-off between detection and discrimination (Olsen et al., 2012; Guo et al., 2017;

Ibrahim et al., 2021). In practical terms, the CT pathway may be elevating the “signal” and suppressing the “noise”: it reduces spurious activity to trivial stimuli (or spontaneous activity from a damaged cochlea) and ensures that meaningful auditory cues still evoke strong cortical responses. Such a mechanism would preserve perceptual stability and potentially improve functions like speech understanding in noisy environments.

ETs likely ensure that the overall drive to subcortical auditory structures is maintained. Even though ETs did not markedly change their own excitability, their transient shift to favor responsiveness to lower frequency sounds and the putative recruitment of intracortical inputs allow them to continue sending signals to downstream nuclei. By preserving ET activity, the ACtx guarantees that key downstream centers remain engaged and active during the critical period after injury. ET circuits provide a broad corticofugal output and are crucial for high-level cognitive processes, acoustic-motor behaviors, and auditory plasticity (Bajo et al., 2010; Li et al., 2021; Souffi et al., 2021; Lesicko and Geffen, 2022). Thus, this sustained subcortical drive could itself trigger adaptive plasticity in those centers.

It should be noted that although these mechanisms are aimed at preserving hearing function after cochlear damage, they operate on a delicate balance. Even within ostensibly homeostatic/compensatory changes, there is a risk of overcompensation, hyperactivity and thalamocortical dysrhythmia, which can contribute to disorders like tinnitus and hyperacusis (Llinas et al., 2005; Henton and Tzounopoulos, 2021; Smith et al., 2025)

In conclusion, our work reveals cell-type-specific plasticity in ACtx ETs and CTs following noise trauma. The observed changes in synaptic strength, intrinsic properties, and sound response tuning suggest a coordinated adaptive response aimed at preserving auditory function directly or via triggering adaptive plasticity in MGB and the ACtx. These findings contribute to a broader understanding of cortical plasticity in sensory processing and may inform therapeutic strategies for enhancing recovery from hearing loss and mitigating hearing loss-related disorders, such as tinnitus and hyperacusis.

Funding
This work was supported by NIH grants R01-DC019618 (TT), R01-DC020923 (TT), R21-DC018327 (RSW), R01-DC020459 (RSW), a Hearing Health Foundation Emerging Research Grant (RSW), and a Klingenstein-Simons Fellowship in Neuroscience (RSW).

Acknowledgements
We thank current and former members of the Tzounopoulos and Williamson Labs for helpful feedback and discussions, and assistance with animal care.

Author Contributions
Conceptualization: TT/RSW/SK
Methodology: YZ/SK/NAS/SL/MPA
Validation: YZ/SK/NAS/RFK/SL
Formal analysis: YZ/SK/NAS/RFK
Investigation: YZ/SK/NAS/RFK/SL
Writing - original draft: TT/RSW/SK
Writing - review & editing: YZ/SK/NAS/TT/RSW/MPA
Supervision: TT/RSW
Funding acquisition: TT/RSW

Figure Legends

Figure 1. Transient shift in TC synaptic strength from CT and ET equivalent to CT dominant one day after NE.

(A) Schematic illustration of stereotaxic injections of retrograde microspheres to label L5 extratelencephalic neurons (ETs, green), and viral vectors (AAVs) for expression of ChR2 in thalamocortical (TC) inputs and tdTomato in L6 corticothalamic neurons (CTs, red) in Ntsr1-Cre mice.

(B) Schematic illustration of slice electrophysiology experiment involving photostimulation of ChR2 expressing TC afferents and simultaneous (dual) recording from an ET (green) and a CT (red).

(C) Images in 4X magnification showing the extent of ACtx area in bright-field (left), green-labeled ETs and TC axons (middle) and red-labeled CTs.

(D) Average CT/ET EPSC ratio after optogenetically stimulating thalamic L5-6 input 1d and 7d after SE and NE. (1d SE: 18 cells/6 mice; 1d NE: 26 cells/9 mice; 7d SE: 10 cells/6 mice; 7d NE: 10 cells/6 mice). Asterisks indicate significant differences (***$p<0.001$, two-way ANOVA and Bonferroni correction for multiple comparisons).

(E, F) Representative traces of EPSCs in dual recordings from both CT (solid line) and ET (dotted line) neurons evoked by maximal photostimulation of L5-6 thalamocortical inputs in 1d SE (E, left) and 1d NE (E, right); 7d SE (F, left) and 7d NE (F, right). Different colored traces represent different pairs of simultaneously recorded CTs and ETs.

Detailed statistical values are listed in Table 1.

828 **Figure 2. Transient increase in the *q* of TC→CT synapses 1 day after NE.**
829 **(A, C)** Average amplitude of light-evoked quantal EPSCs (Sr^{2+}-mEPSCs) in CTs in response to
830 L5-6 thalamocortical maximal photostimulation in 1d (A) and 7d (C), post SE (black) and NE (red)
831 mice (1d SE: 7 cells/3 mice; 1d NE: 6 cells/3 mice; 7d SE: 5 cells/2 mice; 7d NE: 6 cells/2 mice).
832 Asterisks indicate significant differences (*$p<0.05$, unpaired t-test).
833 **(B, D)** Representative Sr^{2+}-mEPSCs traces (top left) and representative average traces of quantal
834 Sr^{2+}-mEPSCs traces (top right). Amplitude histogram of events before (background noise) and
835 after stimulation from the same cell (bottom) in 1d (B) and 7d (D) after SE (black) and NE (red)
836 mice. The arrowhead indicates the onset of light stimulus. The dotted line indicates 400ms time
837 window before stimulus (pre-LED). The solid line represents a 400ms time window, which started
838 100 ms after the stimulus (post-LED) and was used to analyze the amplitude of Sr^{2+}-mEPSCs (1d
839 SE: 7 cells/3 mice; 1d NE: 6 cells/3 mice; 7d SE: 5 cells/2 mice; 7d NE: 6 cells/2 mice).
840 **(E, G)** Summary graph of the average CT EPSC amplitudes in response to L5-6 thalamocortical
841 maximal photostimulation in 1d (E) and 7d (G) SE (black) and NE (red). (1d SE: 18 cells/6 mice;
842 1d NE: 26 cells/9 mice; 7d SE: 10 cells/6 mice; 7d NE: 10 cells/6 mice). Asterisks indicate
843 significant differences (**$p<0.01$, Mann-Whitney U test).
844 **(F, H)** Representative traces of L6 CT EPSCs in response to L5-6 thalamocortical maximal
845 photostimulation in 1d SE (F, black line) and 1d NE (F, red line) and 7d SE (H, black line) and 7d
846 NE (H, red line).
847 Detailed statistical values are listed in Table 1.
848
849

850 **Figure 3. Transient increase in suprathreshold CT intrinsic excitability 1 day after NE.**
851 **(A)** Average CT input resistance (R_{input}) 1d and 7d after SE (black) or NE (red) (1d SE: 22 cells/8
852 mice; 1d NE: 23 cells/5 mice; 7d SE: 23 cells/6 mice; 7d NE: 21 cells/4 mice).
853 **(B)** Average CT resting membrane potential (V_{rest}) 1d and 7d after SE (black) or NE (red) (1d SE:
854 22 cells/8 mice; 1d NE: 23 cells/5 mice; 7d SE: 23 cells/6 mice; 7d NE: 21 cells/4 mice).
855 **(C)** Average CT AP width 1d and 7d after SE (black) or NE (red) (1d SE: 21 cells/8 mice; 1d NE:
856 21 cells/5 mice; 7d SE: 23 cells/6 mice; 7d NE: 21 cells/4 mice).
857 **(D)** Average CT AP threshold of 1d and 7d after SE (black) or NE (red) (1d SE: 21 cells/8 mice;
858 1d NE: 19 cells/5 mice; 7d SE: 23 cells/6 mice; 7d NE: 21 cells/4 mice).
859 **(E, G)** Representative traces of CT firing in response to depolarizing current (50, 100, 200 pA
860 current injections), 1d SE (E, left) vs. 1d NE (E, right); and 7d SE (G, left) vs. 7d NE (G, right).
861 **(F, H)** Average firing frequency as a function of injected current amplitude, 1d SE vs. 1d NE (F),
862 and 7d SE vs. 7d NE (H). Current injections from 25 to 250 pA with an increment of 25 pA (1d
863 SE: 21 cells/8 mice; 1d NE: 21 cells/5 mice; 7d SE: 23 cells/6 mice; 7d NE: 21 cells/4 mice).
864 Asterisks indicate significant differences (**$p<0.01$, two-way ANOVA and Bonferroni correction
865 for multiple comparisons).
866 Detailed statistical values are listed in Table 1.
867
868

Figure 4. No changes in the *q* of TC→ET synapses after NE.

(A, C) Average amplitude of Sr^{2+}-mEPSCs in ETs in response to L5-6 thalamocortical maximal photostimulation in 1d (A) and 7d (C), post SE (black) and NE (red) (1d SE: 5 cells/4 mice; 1d NE: 7 cells/5 mice; 7d SE: 7 cells/2 mice; 7d NE: 5 cells/2 mice).

(B, D) Representative Sr^{2+}-mEPSCs traces (top left) and representative average traces of quantal Sr^{2+}-mEPSCs traces (top right). Amplitude histogram of events before (background noise) and after stimulation from the same cell (bottom) in 1d (B) and 7d (D) after SE (black) and NE (red) mice. The arrowhead indicates the onset of light stimulus. The dotted line indicates 400ms time window before stimulus (pre-LED). The solid line represents a 400ms time window, which started 100 ms after the stimulus (post-LED) and was used to analyze the amplitude of Sr^{2+}-mEPSCs (1d SE: 5 cells/4 mice; 1d NE: 7 cells/5 mice; 7d SE: 7 cells/2 mice; 7d NE: 5 cells/2 mice).

(E, G) Summary graph of the average L5 ET EPSC amplitudes in response to L5-6, and L1-4 thalamocortical maximal photostimulation in 1d SE vs. 1d NE, or 7d SE vs. 7d NE mice (L5-6: 1d SE: 18 cells/6 mice; 1d NE: 26 cells/9 mice; 7d SE: 10 cells/6 mice; 7d NE: 10 cells/6 mice; L1-4: 1d SE: 8 cells/3 mice; 1d NE: 7 cells/4 mice; 7d SE: 9 cells/5 mice; 7d NE: 12 cells/4 mice).

(F, H) Representative traces of L5 ET EPSCs in response to L5-6, and L1-4 thalamocortical maximal photostimulation in 1d SE (F left, H left, black) vs. 1d NE (F left, H left, red), 7d SE (F right, H right, black) vs. 7d NE (F right, H right, red) mice.

Detailed statistical values are listed in Table 1.

890 **Figure 5. No changes in ET intrinsic excitability after NE.**
891 **(A)** Average ET R_{input} 1d and 7d after SE (black) or NE (red) (1d SE: 21 cells/6 mice; 1d NE: 21
892 cells/5 mice; 7d SE: 20 cells/5 mice; 7d NE: 23 cells/6 mice).
893 **(B)** Average ET V_{rest} 1d and 7d after SE (black) or NE (red) (1d SE: 21 cells/6 mice; 1d NE: 21
894 cells/5 mice; 7d SE: 20 cells/5 mice; 7d NE: 23 cells/6 mice).
895 **(C)** Average ET AP width 1d and 7d after SE (black) or NE (red) (1d SE: 21 cells/6 mice; 1d NE:
896 21 cells/5 mice; 7d SE: 20 cells/5 mice; 7d NE: 23 cells/6 mice).
897 **(D)** Average ET AP threshold 1d and 7d after SE (black) or NE (red) (1d SE: 21 cells/6 mice; 1d
898 NE: 21 cells/5 mice; 7d SE: 20 cells/5 mice; 7d NE: 23 cells/6 mice).
899 **(E, G)** Representative traces of ET firing in response to depolarizing current injection (50, 100,
900 200 pA), 1d SE (E, left) vs. 1d NE (E, right); and 7d SE (G, left) vs. 7d NE (G, right).
901 **(F, H)** Average firing frequency as a function of injected current amplitude, 1d SE vs. 1d NE (F),
902 and 7d SE vs. 7d NE (H). Current injections from 25 to 350 pA with an increment of 25 pA. (1d
903 SE: 21 cells/6 mice; 1d NE: 20 cells/5 mice; 7d SE: 20 cells/5 mice; 7d NE: 23 cells/6 mice).
904 Detailed statistical values are listed in Table 1.
905
906

Figure 6. Changes in CT sound response responses persist 7 days after NE.
(A) Example two-photon field of view from CTs imaged before and after exposure.
(B) Average responses to pure tones across all CTs in SE mice (-1d: n=507 neurons; 1d: n=460 neurons; 7d: n=432 neurons). Asterisks indicate significant pairwise differences.
(C) Same as (**A**) for NE mice (-1d: n=713 neurons; 1d: n=638 neurons; 7d: n=646 neurons). Asterisks indicate significant pairwise differences.
(D) Tuning curves aligned to best frequency (BF) in SE mice.
(E) Same as (**D**) for NE mice. Asterisks indicate significant pairwise differences (*$p<0.05$, Bonferroni corrected for multiple comparisons).
(F) Change in BF of matched cells in SE (black) and NE (red) mice (1d SE: n=40 neurons; 1d NE: n=36 neurons; 7d SE: n=35 neurons; 7d NE: n=40 neurons).
(G) Accuracy of a multinomial logistic regression classifier trained to decode the frequency of pure tones at 80 dB SPL. Dashed line represents chance level. Error bars represent standard deviation of decoding iterations.
(H) Average responses to white noise bursts at different intensities across all ETs in SE mice (-1d: n=438 neurons; 1d: n=460 neurons; 7d: n=411 neurons). Asterisks indicate significant pairwise differences (Bonferroni corrected for multiple comparisons).
(I) Same as (**H**) in NE mice (-1d: n=636 neurons; 1d: n=559 neurons; 7d: n=587 neurons). Asterisks indicate significant pairwise differences (Bonferroni corrected for multiple comparisons).
(J) Change in intensity thresholds across days in SE (black) and NE (red) mice (1d SE: n=27 neurons; 1d NE: n=31 neurons; 7d SE: n=29 neurons; 7d NE: n=25 neurons). Asterisks indicate significant pairwise differences (**$p<0.01$, ***$p<0.001$, Bonferroni corrected for multiple comparisons).
(K) Accuracy of a multinomial logistic regression trained to decode sound intensity. Dashed line represents chance level. Error bars represent standard deviation of decoding iterations.
Detailed statistical values are listed in Table 1.

Figure 7. Transient shift in ET sound response properties one day after NE.
(A) Example two-photon field of view from ETs imaged before and after exposure.
(B) Average responses to pure tones across all ETs in SE mice (-1d: n=385 neurons; 1d: n=414 neurons; 7d: n=400 neurons).
(C) Same as in (**A**) for NE mice (-1d: n=268 neurons; 1d: n=235 neurons; 7d: n=296 neurons). Asterisks indicate significant pairwise differences (Bonferroni corrected for multiple comparisons).
(D) Tuning curves aligned to best frequency (BF) in SE mice.
(E) Same as in (**D**) for NE mice. Asterisks indicate significant pairwise differences (*p<0.05, ****p<0.0001, Bonferroni corrected for multiple comparisons).
(F) Change in BF of matched cells in SE (black) and NE (red) mice (1d SE: n=68 neurons; 1d NE: n=54 neurons; 7d SE: n=68 neurons; 7d NE: n=71 neurons). Asterisks indicate significant pairwise differences (*p<0.05, ****p<0.0001, Bonferroni corrected for multiple comparisons).
(G) Accuracy of a multinomial logistic regression classifier trained to decode the frequency of pure tones at 80 dB SPL. Dashed line represents chance level. Error bars represent standard deviation of decoding iterations. Asterisks indicate significant pairwise differences (*p<0.05, ****p<0.0001, bootstrap test Bonferroni corrected for multiple comparisons).
(H) Average responses to white noise bursts at different intensities across all ETs in SE mice (-1d: n=331 neurons; 1d: n=270 neurons; 7d: n=299 neurons).
(I) Same as (**H**) in NE mice (-1d: n=226 neurons; 1d: n=222 neurons; 7d: n=252 neurons). Asterisks indicate significant pairwise differences (Bonferroni corrected for multiple comparisons).
(J) Change in intensity thresholds across days in SE (black) and NE (red) mice (1d SE: n=42 neurons; 1d NE: n=49 neurons; 7d SE: n=50 neurons; 7d NE: n=51 neurons). Asterisks indicate significant pairwise differences (*p<0.05, **p<0.01, Bonferroni corrected for multiple comparisons).
(K) Accuracy of a multinomial logistic regression trained to decode sound intensity. Dashed line represents chance level. Error bars represent standard deviation of decoding iterations. Asterisks indicate significant pairwise differences (*p<0.05, bootstrap test Bonferroni corrected for multiple comparisons).

967 **Figure 8. Changes in synaptic, intrinsic, and sound response properties correlate with**
968 **the severity of noise trauma.**
969 **(A)** Correlation between ABR click threshold shift and average CT/ET EPSC ratio after
970 optogenetically stimulating thalamic L5-6 input (**Figure 1D**) in 1d SE (black) and NE (red) mice
971 (1d SE: 18 cells/6 mice; 1d NE: 26 cells/9 mice). Line depicts a linear regression of the data
972 points.
973 **(B)** Same as (**A**) for amplitude of light-evoked quantal EPSCs (Sr^{2+}-mEPSCs) in CTs in response
974 to L5-6 thalamocortical maximal photostimulation (**Figure 2A**) in 1d SE (black) and NE (red) mice
975 (1d SE: 7 cells/3 mice; 1d NE: 6 cells/3 mice).
976 **(C)** Same as (**A**) for average CT EPSC amplitudes in response to L5-6 thalamocortical maximal
977 photostimulation (**Figure 2E**) in 1d SE (black) and NE (red) mice (1d SE: 18 cells/6 mice; 1d NE:
978 26 cells/9 mice).
979 **(D)** Same as (**A**) for ET EPSC amplitudes in response to L5-6 thalamocortical maximal
980 photostimulation (**Figure 4E**) in 1d SE (black) and NE (red) mice (1d SE: 18 cells/6 mice; 1d NE:
981 26 cells/9 mice).
982 **(E)** Same as (**A**) for CT resting membrane potential (V_{rest}, **Figure 3B**) in 1d SE (black) and NE
983 (red) mice (1d SE: 22 cells/8 mice; 1d NE: 23 cells/5 mice).
984 **(F)** Same as (**A**) for the maximum firing frequency from the F-I curve (**Figure 3F**) in 1d SE (black)
985 and NE (red) mice (1d SE: 21 cells/8 mice; 1d NE: 21 cells/5 mice).
986 **(G, H)** Same as (**A**) for the change in intensity thresholds (**Figure 6J**) in 1d (**G**) or 7d (**H**) SE
987 (black) and NE (red) mice (1d SE: n=27 neurons; 1d NE: n=31 neurons; 7d SE: n=29 neurons;
988 7d NE: n=25 neurons).
989 **(I, J)** Same as (**A**) for the change in intensity thresholds (**Figure 7J**) in 1d (**I**) or 7d (**J**) SE (black)
990 and NE (red) mice (1d SE: n=42 neurons; 1d NE: n=49 neurons; 7d SE: n=50 neurons; 7d NE:
991 n=51 neurons).
992

Figure S1. Changes in ABR threshold and Wave I amplitude 1 day after NE.
(A) ABR threshold shifts 1d after SE and NE. For clicks and different tone frequencies, 1d SE: 24 mice; 1d NE: 25 mice; Asterisks indicate significant differences (****$p<0.0001$, clicks: Mann-Whitney U test; frequency: two-way ANOVA with Bonferroni correction for multiple comparison).
(B, C) ABR absolute thresholds for 1d NE (B) and 1d SE (C). For clicks and different tone frequencies, -1d NE: 25 mice; 1d NE: 25 mice; -1dSE: 24 mice; 1d SE: 24 mice; Asterisks indicate significant differences (****$p<0.0001$, clicks: Mann-Whitney U test, frequency: two-way ANOVA with Bonferroni correction for multiple comparison).
(D-H) Wave I amplitudes for -1d SE, 1d SE, -1d NE and 1d NE mice for clicks (D), 10 kHz (E), 16 kHz (F), 24 kHz (G) and 32 kHz (H). -1d SE: 14 mice; 1d SE: 14 mice; -1d NE: 14 mice; 1d NE: 14 mice. Detailed statistical values are listed in tables.
(I) Representative traces of ABR recordings (in response to 16 kHz tones) with thresholds highlighted (dotted rectangle) before (left), 1d NE (middle), and 1d SE (right).
Detailed statistical values are listed in Table 2.

Figure S2. Changes in ABR threshold and Wave I amplitude do not recover 7 days after NE.

(A) ABR threshold shifts 7d after SE and NE. For clicks and different tone frequencies, 7d SE: 12 mice; 7d NE: 13 mice; Asterisks indicate significant differences (**p<0.01, clicks, Mann-Whitney U test; ****p<0.0001, frequency, two-way ANOVA with Bonferroni correction for multiple comparison).

(B, C) ABR absolute thresholds in 7d NE (B) and 7d SE (C). For clicks and frequency, -1d NE: 13 mice; 7d NE: 13 mice; -1d SE: 12 mice; 7d SE: 12 mice; Asterisks indicate significant differences (***p<0.001, clicks, Mann-Whitney U test; ****p<0.0001, frequency, mixed-effects with Bonferroni correction for multiple comparison).

(D-H) Wave I amplitudes between -1d -SE, 7d SE, -1d -NE and 7d NE for clicks (D), 10 kHz (E), 16 kHz (F), 24 kHz (G) and 32 kHz (H). -1d -SE: 6 mice; 1d SE: 6 mice; -1d NE: 6 mice; 7d NE: 6 mice.

Detailed statistical values are listed in Table 2.

Figure S3. Two-photon imaging spike deconvolution pipeline.
(A) An example trace comparing the recorded calcium signal to the deconvolved trace used for analysis.
(B) Two example CT neuron responses to frequency stimuli and their intensity-averaged tuning curves. Light grey curves indicate individual trials, and the colored trace shows the average stimulus response.

Figure S4. Increases in absolute intensity thresholds recover in ET neurons but remain elevated in CT neurons.

(A) CTs Intensity thresholds across days in SE (black) and NE (red) mice (-1d SE: n=66 neurons; -1d NE: n=71 neurons; 1d SE: n=27 neurons; 1d NE: n=31 neurons; 7d SE: n=29 neurons; 7d NE: n=25 neurons). Asterisks indicate significant pairwise differences (*$p<0.05$, Bonferroni corrected for multiple comparisons).

(B) ETs intensity thresholds across days in SE (black) and NE (red) mice (-1d SE: n=66 neurons; -1d NE: n=67 neurons; 1d SE: n=42 neurons; 1d NE: n=49 neurons; 7d SE: n=50 neurons; 7d NE: n=51 neurons). Asterisks indicate significant pairwise differences (*$p<0.05$, **$p<0.01$, Bonferroni corrected for multiple comparisons).

Detailed statistical values are listed in Table 2.

References

Asokan MM, Williamson RS, Hancock KE, Polley DB (2018) Sensory overamplification in layer 5 auditory corticofugal projection neurons following cochlear nerve synaptic damage. Nat Commun 9:2468.

Auerbach BD, Rodrigues PV, Salvi RJ (2014) Central gain control in tinnitus and hyperacusis. Front Neurol 5:206.

Bajo VM, Nodal FR, Moore DR, King AJ (2010) The descending corticocollicular pathway mediates learning-induced auditory plasticity. Nat Neurosci 13:253-260.

Chambers AR, Resnik J, Yuan Y, Whitton JP, Edge AS, Liberman MC, Polley DB (2016) Central Gain Restores Auditory Processing following Near-Complete Cochlear Denervation. Neuron 89:867-879.

Chen X, Sun YC, Zhan H, Kebschull JM, Fischer S, Matho K, Huang ZJ, Gillis J, Zador AM (2019) High-Throughput Mapping of Long-Range Neuronal Projection Using In Situ Sequencing. Cell 179:772-786 e719.

Clayton KK, Williamson RS, Hancock KE, Tasaka GI, Mizrahi A, Hackett TA, Polley DB (2021) Auditory Corticothalamic Neurons Are Recruited by Motor Preparatory Inputs. Curr Biol 31:310-321 e315.

Day ML, Delgutte B (2016) Neural population encoding and decoding of sound source location across sound level in the rabbit inferior colliculus. J Neurophysiol 115:193-207.

Ford AN, Czarny JE, Rogalla MM, Quass GL, Apostolides PF (2024) Auditory Corticofugal Neurons Transmit Auditory and Non-auditory Information During Behavior. J Neurosci 44.

Gilbert CD, Wiesel TN (1992) Receptive field dynamics in adult primary visual cortex. Nature 356:150-152.

Guo W, Clause AR, Barth-Maron A, Polley DB (2017) A Corticothalamic Circuit for Dynamic Switching between Feature Detection and Discrimination. Neuron 95:180-194 e185.

Harris KD, Shepherd GM (2015) The neocortical circuit: themes and variations. Nat Neurosci 18:170-181.

Henton A, Tzounopoulos T (2021) What's the buzz? The neuroscience and the treatment of tinnitus. Physiol Rev 101:1609-1632.

Hooks BM, Mao T, Gutnisky DA, Yamawaki N, Svoboda K, Shepherd GM (2013) Organization of cortical and thalamic input to pyramidal neurons in mouse motor cortex. J Neurosci 33:748-760.

Ibrahim BA, Murphy CA, Yudintsev G, Shinagawa Y, Banks MI, Llano DA (2021) Corticothalamic gating of population auditory thalamocortical transmission in mouse. Elife 10.

Issa LK, Sekaran NVC, Llano DA (2023) Highly branched and complementary distributions of layer 5 and layer 6 auditory corticofugal axons in mouse. Cereb Cortex 33:9566-9582.

Ji XY, Zingg B, Mesik L, Xiao Z, Zhang LI, Tao HW (2016) Thalamocortical Innervation Pattern in Mouse Auditory and Visual Cortex: Laminar and Cell-Type Specificity. Cereb Cortex 26:2612-2625.

Jones EG (1998) Viewpoint: the core and matrix of thalamic organization. Neuroscience 85:331-345.

Jones EG (2001) The thalamic matrix and thalamocortical synchrony. Trends Neurosci 24:595-601.

Joshi A, Kalappa BI, Anderson CT, Tzounopoulos T (2016) Cell-Specific Cholinergic Modulation of Excitability of Layer 5B Principal Neurons in Mouse Auditory Cortex. J Neurosci 36:8487-8499.

Joshi A, Middleton JW, Anderson CT, Borges K, Suter BA, Shepherd GM, Tzounopoulos T (2015) Cell-specific activity-dependent fractionation of layer 2/3-->5B excitatory signaling in mouse auditory cortex. J Neurosci 35:3112-3123.
Kaas JH, Krubitzer LA, Chino YM, Langston AL, Polley EH, Blair N (1990) Reorganization of retinotopic cortical maps in adult mammals after lesions of the retina. Science 248:229-231.
Katz LC, Iarovici DM (1990) Green fluorescent latex microspheres: a new retrograde tracer. Neuroscience 34:511-520.
Kotak VC, Fujisawa S, Lee FA, Karthikeyan O, Aoki C, Sanes DH (2005) Hearing loss raises excitability in the auditory cortex. J Neurosci 25:3908-3918.
Kouvaros S, Kumar M, Tzounopoulos T (2020) Synaptic Zinc Enhances Inhibition Mediated by Somatostatin, but not Parvalbumin, Cells in Mouse Auditory Cortex. Cereb Cortex 30:3895-3909.
Kouvaros S, Bizup B, Solis O, Kumar M, Ventriglia E, Curry FP, Michaelides M, Tzounopoulos T (2023) A CRE/DRE dual recombinase transgenic mouse reveals synaptic zinc-mediated thalamocortical neuromodulation. Sci Adv 9:eadf3525.
Kujawa SG, Liberman MC (2009) Adding insult to injury: cochlear nerve degeneration after "temporary" noise-induced hearing loss. J Neurosci 29:14077-14085.
Kullander K, Topolnik L (2021) Cortical disinhibitory circuits: cell types, connectivity and function. Trends Neurosci 44:643-657.
Kumar M, Handy G, Kouvaros S, Zhao Y, Brinson LL, Wei E, Bizup B, Doiron B, Tzounopoulos T (2023) Cell-type-specific plasticity of inhibitory interneurons in the rehabilitation of auditory cortex after peripheral damage. Nat Commun 14:4170.
Larkum M (2013) A cellular mechanism for cortical associations: an organizing principle for the cerebral cortex. Trends Neurosci 36:141-151.
Lesicko AMH, Geffen MN (2022) Diverse functions of the auditory cortico-collicular pathway. Hear Res 425:108488.
Letzkus JJ, Wolff SB, Meyer EM, Tovote P, Courtin J, Herry C, Luthi A (2011) A disinhibitory microcircuit for associative fear learning in the auditory cortex. Nature 480:331-335.
Li Z, Wei JX, Zhang GW, Huang JJ, Zingg B, Wang X, Tao HW, Zhang LI (2021) Corticostriatal control of defense behavior in mice induced by auditory looming cues. Nat Commun 12:1040.
Liberman MC, Dodds LW (1984) Single-neuron labeling and chronic cochlear pathology. III. Stereocilia damage and alterations of threshold tuning curves. Hear Res 16:55-74.
Llano DA, Sherman SM (2008) Evidence for nonreciprocal organization of the mouse auditory thalamocortical-corticothalamic projection systems. J Comp Neurol 507:1209-1227.
Llinas R, Urbano FJ, Leznik E, Ramirez RR, van Marle HJ (2005) Rhythmic and dysrhythmic thalamocortical dynamics: GABA systems and the edge effect. Trends Neurosci 28:325-333.
Lur G, Vinck MA, Tang L, Cardin JA, Higley MJ (2016) Projection-Specific Visual Feature Encoding by Layer 5 Cortical Subnetworks. Cell Rep 14:2538-2545.
Mease RA, Krieger P, Groh A (2014) Cortical control of adaptation and sensory relay mode in the thalamus. Proc Natl Acad Sci U S A 111:6798-6803.
Merzenich MM, Kaas JH, Wall J, Nelson RJ, Sur M, Felleman D (1983) Topographic reorganization of somatosensory cortical areas 3b and 1 in adult monkeys following restricted deafferentation. Neuroscience 8:33-55.
Nogueira I, Lima TZ, Malfatti T, Leao KE (2023) Loud noise-exposure changes the firing frequency of subtypes of layer 5 pyramidal neurons and Martinotti cells in the mouse auditory cortex. Front Aging Neurosci 15:1152497.
Oliet SH, Malenka RC, Nicoll RA (1996) Bidirectional control of quantal size by synaptic activity in the hippocampus. Science 271:1294-1297.

Olsen SR, Bortone DS, Adesnik H, Scanziani M (2012) Gain control by layer six in cortical circuits of vision. Nature 483:47-52.
Pachitariu M SC, Dipoppa M, Schröder S, Rossi LF (2016) Suite2p : beyond 10 , 000 neurons with standard two-photon microscopy. bioRxiv:1-30.
Pfeffer CK, Xue M, He M, Huang ZJ, Scanziani M (2013) Inhibition of inhibition in visual cortex: the logic of connections between molecularly distinct interneurons. Nat Neurosci 16:1068-1076.
Qiu C, Salvi R, Ding D, Burkard R (2000) Inner hair cell loss leads to enhanced response amplitudes in auditory cortex of unanesthetized chinchillas: evidence for increased system gain. Hear Res 139:153-171.
Quass GL, Rogalla MM, Ford AN, Apostolides PF (2024) Mixed Representations of Sound and Action in the Auditory Midbrain. J Neurosci 44.
Rasmusson DD (1982) Reorganization of raccoon somatosensory cortex following removal of the fifth digit. J Comp Neurol 205:313-326.
Resnik J, Polley DB (2017) Fast-spiking GABA circuit dynamics in the auditory cortex predict recovery of sensory processing following peripheral nerve damage. Elife 6.
Resnik J, Polley DB (2021) Cochlear neural degeneration disrupts hearing in background noise by increasing auditory cortex internal noise. Neuron.
Robertson D, Irvine DR (1989) Plasticity of frequency organization in auditory cortex of guinea pigs with partial unilateral deafness. J Comp Neurol 282:456-471.
Romero S, Hight AE, Clayton KK, Resnik J, Williamson RS, Hancock KE, Polley DB (2020) Cellular and Widefield Imaging of Sound Frequency Organization in Primary and Higher Order Fields of the Mouse Auditory Cortex. Cereb Cortex 30:1603-1622.
Ryan A, Bone RC (1978) Noise-induced threshold shift and cochlear pathology in the Mongolian gerbil. J Acoust Soc Am 63:1145-1151.
Sarro EC, Kotak VC, Sanes DH, Aoki C (2008) Hearing loss alters the subcellular distribution of presynaptic GAD and postsynaptic GABAA receptors in the auditory cortex. Cereb Cortex 18:2855-2867.
Scholl B, Wehr M (2008) Disruption of balanced cortical excitation and inhibition by acoustic trauma. J Neurophysiol 100:646-656.
Seki S, Eggermont JJ (2003) Changes in spontaneous firing rate and neural synchrony in cat primary auditory cortex after localized tone-induced hearing loss. Hear Res 180:28-38.
Shepherd GMG, Yamawaki N (2021) Untangling the cortico-thalamo-cortical loop: cellular pieces of a knotty circuit puzzle. Nat Rev Neurosci 22:389-406.
Sherman SM (2007) The thalamus is more than just a relay. Current Opinion in Neurobiology 17:417-422.
Smith SS, Jahn KN, Sugai JA, Hancock KE, Polley DB (2025) Objective autonomic signatures of tinnitus and sound sensitivity disorders. Sci Transl Med 17:eadp1934.
Souffi S, Nodal FR, Bajo VM, Edeline JM (2021) When and How Does the Auditory Cortex Influence Subcortical Auditory Structures? New Insights About the Roles of Descending Cortical Projections. Front Neurosci 15:690223.
Stebbings KA, Lesicko AM, Llano DA (2014) The auditory corticocollicular system: molecular and circuit-level considerations. Hear Res 314:51-59.
Super H, Spekreijse H, Lamme VA (2001) Two distinct modes of sensory processing observed in monkey primary visual cortex (V1). Nat Neurosci 4:304-310.
Takesian AE, Kotak VC, Sharma N, Sanes DH (2013) Hearing loss differentially affects thalamic drive to two cortical interneuron subtypes. J Neurophysiol 110:999-1008.
Tononi G, Edelman GM (1998) Consciousness and complexity. Science 282:1846-1851.
Tononi G, Edelman GM, Sporns O (1998) Complexity and coherency: integrating information in the brain. Trends Cogn Sci 2:474-484.

1195 Whitt JL, Ewall G, Chakraborty D, Adegbesan A, Lee R, Kanold PO, Lee HK (2022) Visual
1196 Deprivation Selectively Reduces Thalamic Reticular Nucleus-Mediated Inhibition of the
1197 Auditory Thalamus in Adults. J Neurosci 42:7921-7930.
1198 Williamson RS, Polley DB (2019) Parallel pathways for sound processing and functional
1199 connectivity among layer 5 and 6 auditory corticofugal neurons. Elife 8.
1200 Winer JA (2005) Decoding the auditory corticofugal systems. Hear Res 207:1-9.
1201 Xiong XR, Liang F, Zingg B, Ji XY, Ibrahim LA, Tao HW, Zhang LI (2015) Auditory cortex
1202 controls sound-driven innate defense behaviour through corticofugal projections to
1203 inferior colliculus. Nat Commun 6:7224.
1204 Yamawaki N, Shepherd GM (2015) Synaptic circuit organization of motor corticothalamic
1205 neurons. J Neurosci 35:2293-2307.
1206 Yamawaki N, Raineri Tapies MG, Stults A, Smith GA, Shepherd GM (2021) Circuit organization
1207 of the excitatory sensorimotor loop through hand/forelimb S1 and M1. Elife 10.
1208 Yang S, Weiner BD, Zhang LS, Cho SJ, Bao S (2011) Homeostatic plasticity drives tinnitus
1209 perception in an animal model. Proc Natl Acad Sci U S A 108:14974-14979.
1210

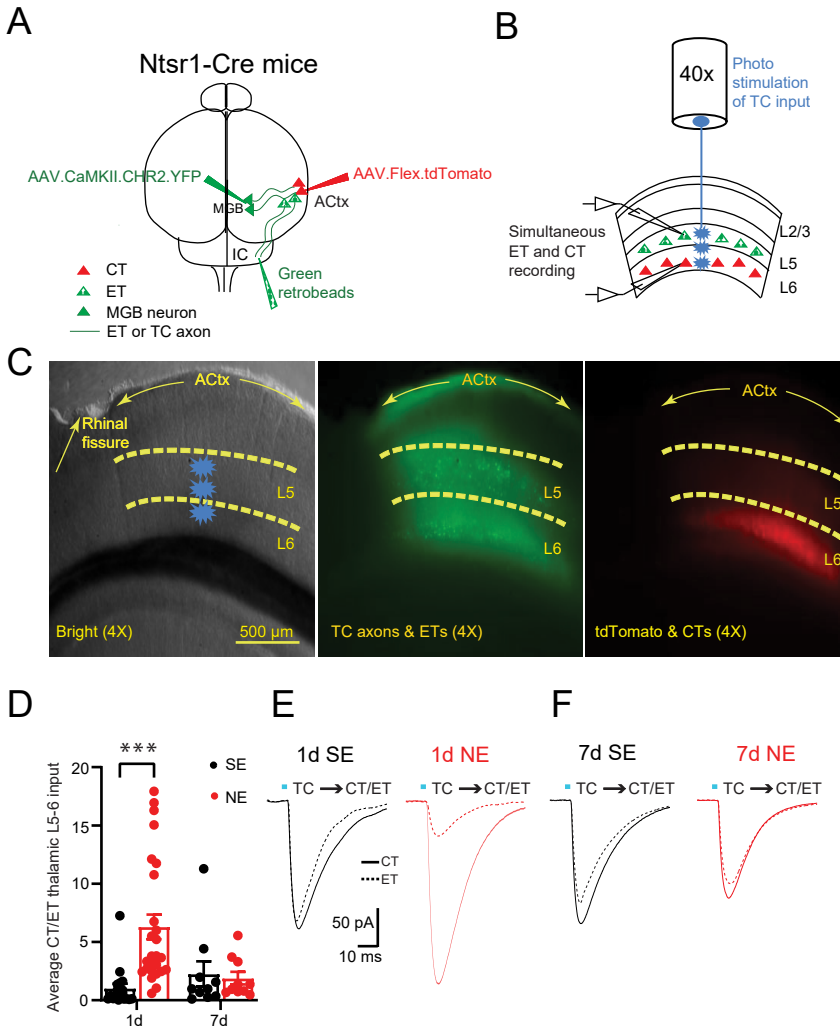
A
Ntsr1-Cre mice
AAV.CaMKII.CHR2.YFP
AAV.Flex.tdTomato
MGB
ACtx
IC
Green retrobeads
CT
ET
MGB neuron
ET or TC axon
B
40x
Photo stimulation of TC input
Simultaneous ET and CT recording
L2/3
L5
L6
C
ACtx
Rhinal fissure
L5
L6
Bright (4X)
500 µm
TC axons & ETs (4X)
tdTomato & CTs (4X)
D
Average CT/ET thalamic L5-6 input
***
SE
NE
1d
7d
E
1d SE
1d NE
TC → CT/ET
CT
ET
50 pA
10 ms
F
7d SE
7d NE

Figure 1

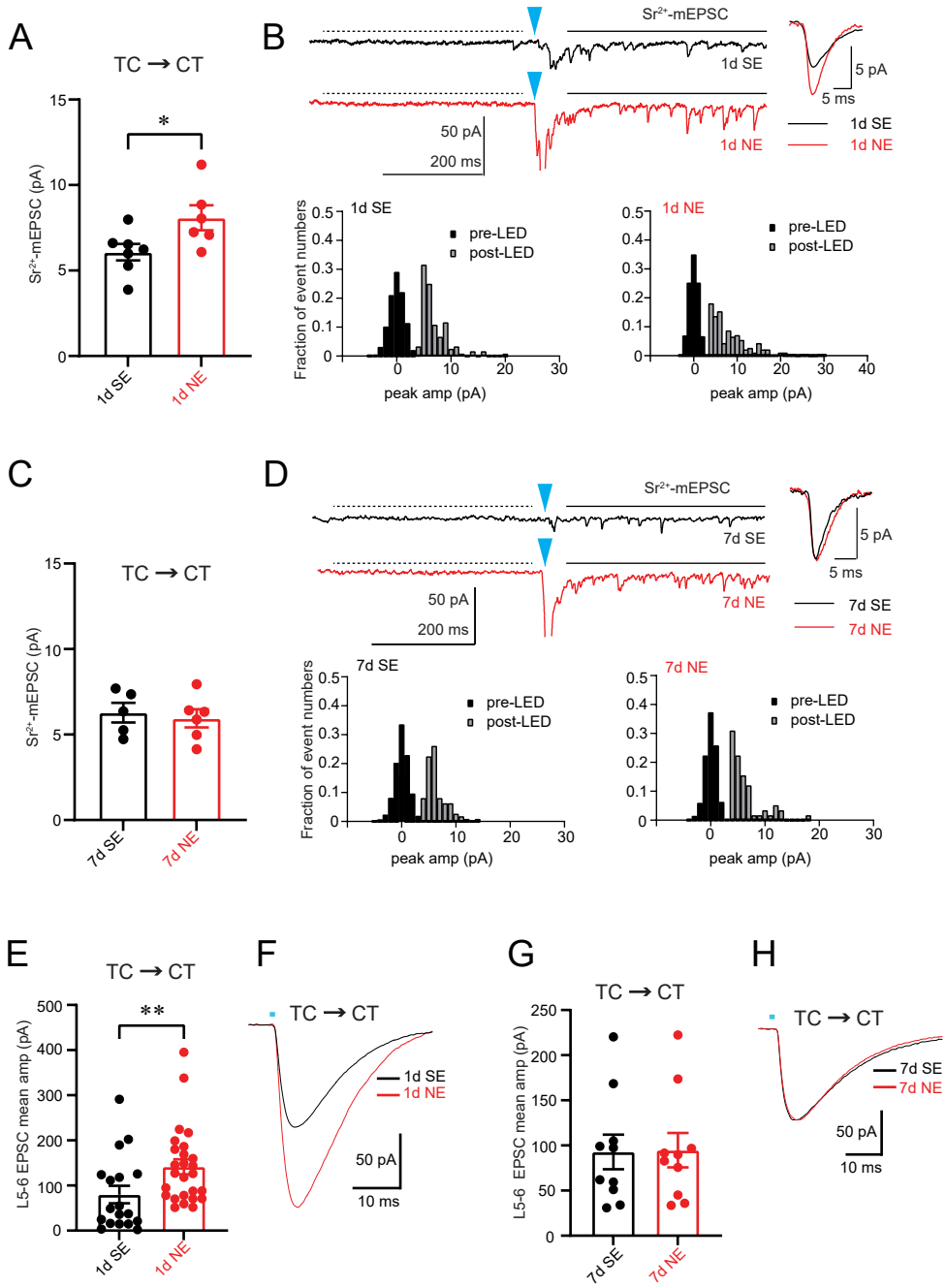
A
TC → CT
Sr2+-mEPSC (pA)
1d SE
1d NE
B
Sr2+-mEPSC
1d SE
1d NE
50 pA
200 ms
5 pA
5 ms
Fraction of event numbers
pre-LED
post-LED
peak amp (pA)
C
7d SE
7d NE
D
E
L5-6 EPSC mean amp (pA)
F
G
H

Figure 2

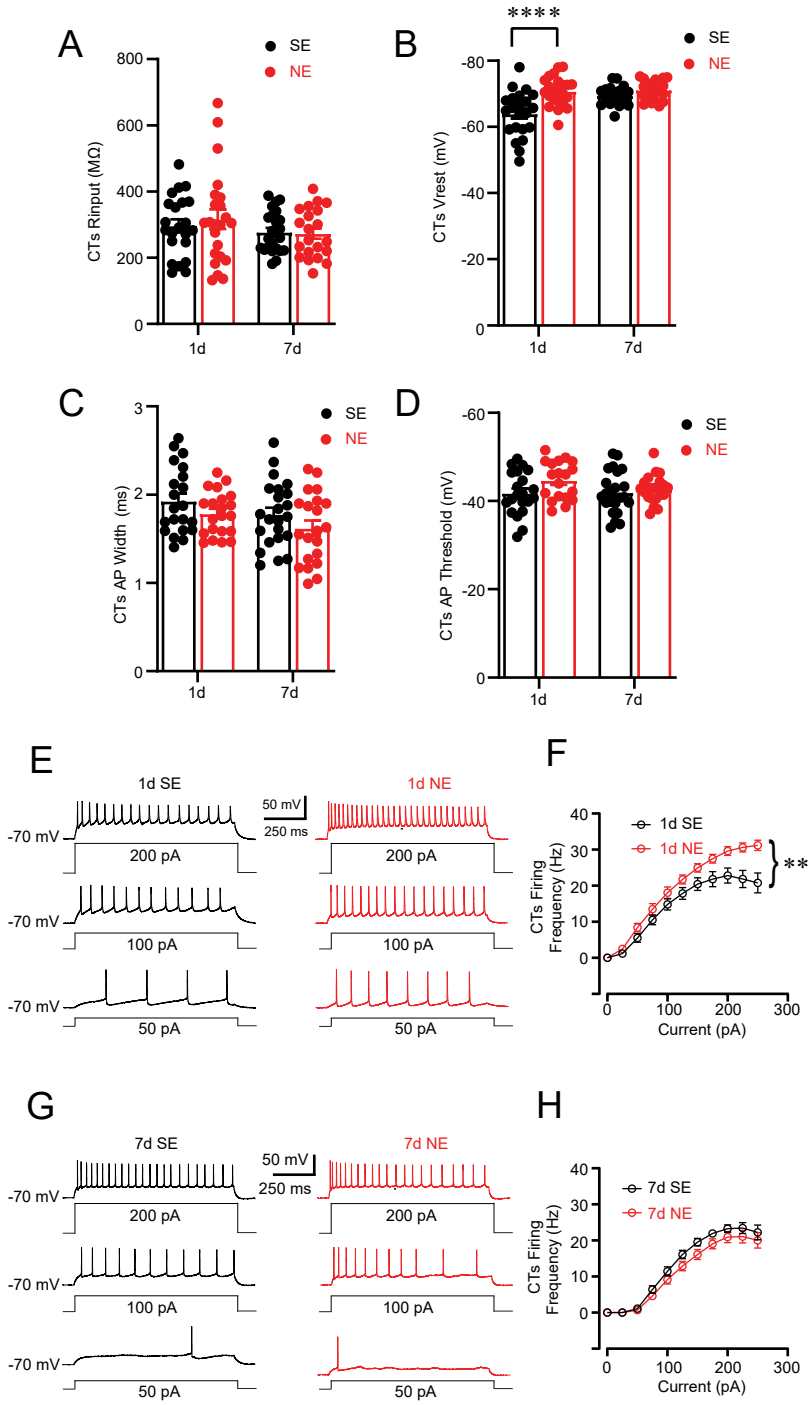
A
SE
NE
CTs Rinput (MΩ)
800
600
400
200
0
1d
7d
B
****
SE
NE
CTs Vrest (mV)
-80
-60
-40
-20
0
1d
7d
C
SE
NE
CTs AP Width (ms)
3
2
1
0
1d
7d
D
SE
NE
CTs AP Threshold (mV)
-60
-40
-20
0
1d
7d
E
1d SE
1d NE
50 mV
250 ms
-70 mV
200 pA
100 pA
50 pA
F
1d SE
1d NE
CTs Firing Frequency (Hz)
40
30
20
10
0
**
0
100
200
300
Current (pA)
G
7d SE
7d NE
50 mV
250 ms
-70 mV
200 pA
100 pA
50 pA
H
7d SE
7d NE
CTs Firing Frequency (Hz)
40
30
20
10
0
0
100
200
300
Current (pA)

Figure 3

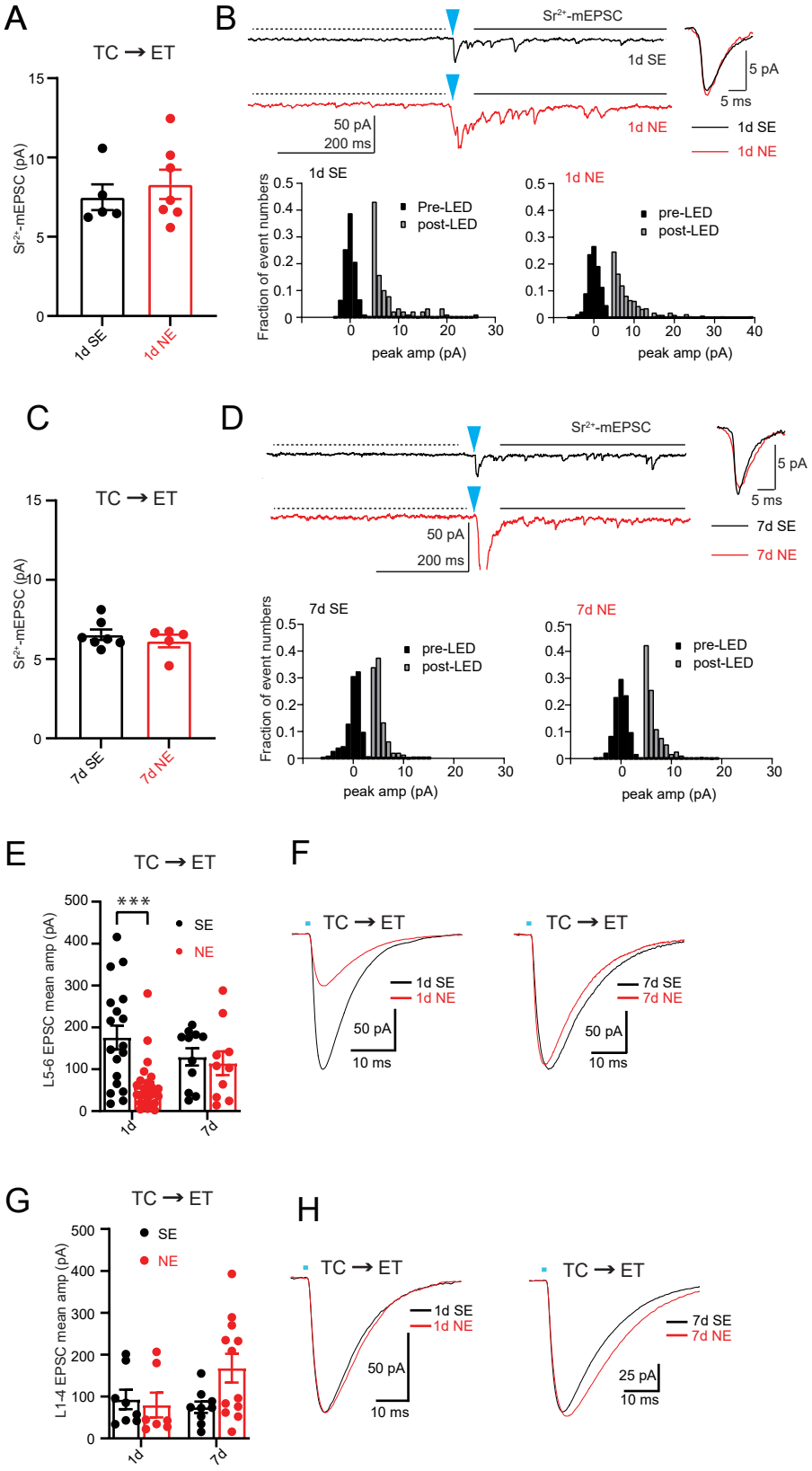
A
TC → ET
Sr2+-mEPSC (pA)
1d SE
1d NE
B
Sr2+-mEPSC
1d SE
1d NE
5 pA
5 ms
50 pA
200 ms
Fraction of event numbers
Pre-LED
post-LED
peak amp (pA)
C
7d SE
7d NE
D
7d SE
7d NE
E
L5-6 EPSC mean amp (pA)
SE
NE
1d
7d
F
G
L1-4 EPSC mean amp (pA)
H
25 pA

Figure 4

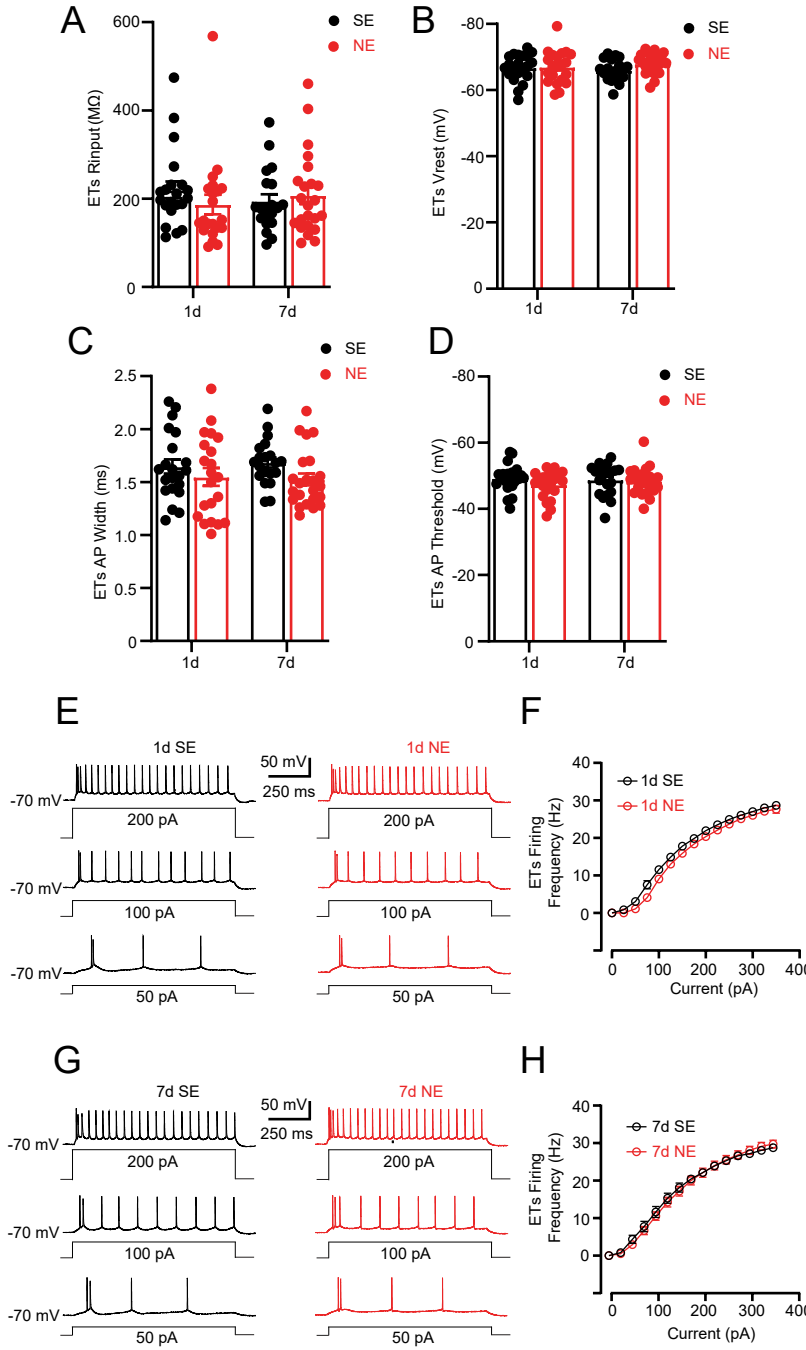
A
ETs Rinput (MΩ)
600
400
200
0
1d
7d
SE
NE
B
ETs Vrest (mV)
-80
-60
-40
-20
0
1d
7d
SE
NE
C
ETs AP Width (ms)
2.5
2.0
1.5
1.0
0.5
0
1d
7d
SE
NE
D
ETs AP Threshold (mV)
-80
-60
-40
-20
0
1d
7d
SE
NE
E
1d SE
1d NE
50 mV
250 ms
-70 mV
200 pA
100 pA
50 pA
F
ETs Firing Frequency (Hz)
40
30
20
10
0
1d SE
1d NE
0
100
200
300
400
Current (pA)
G
7d SE
7d NE
50 mV
250 ms
-70 mV
200 pA
100 pA
50 pA
H
ETs Firing Frequency (Hz)
40
30
20
10
0
7d SE
7d NE
0
100
200
300
400
Current (pA)

Figure 5

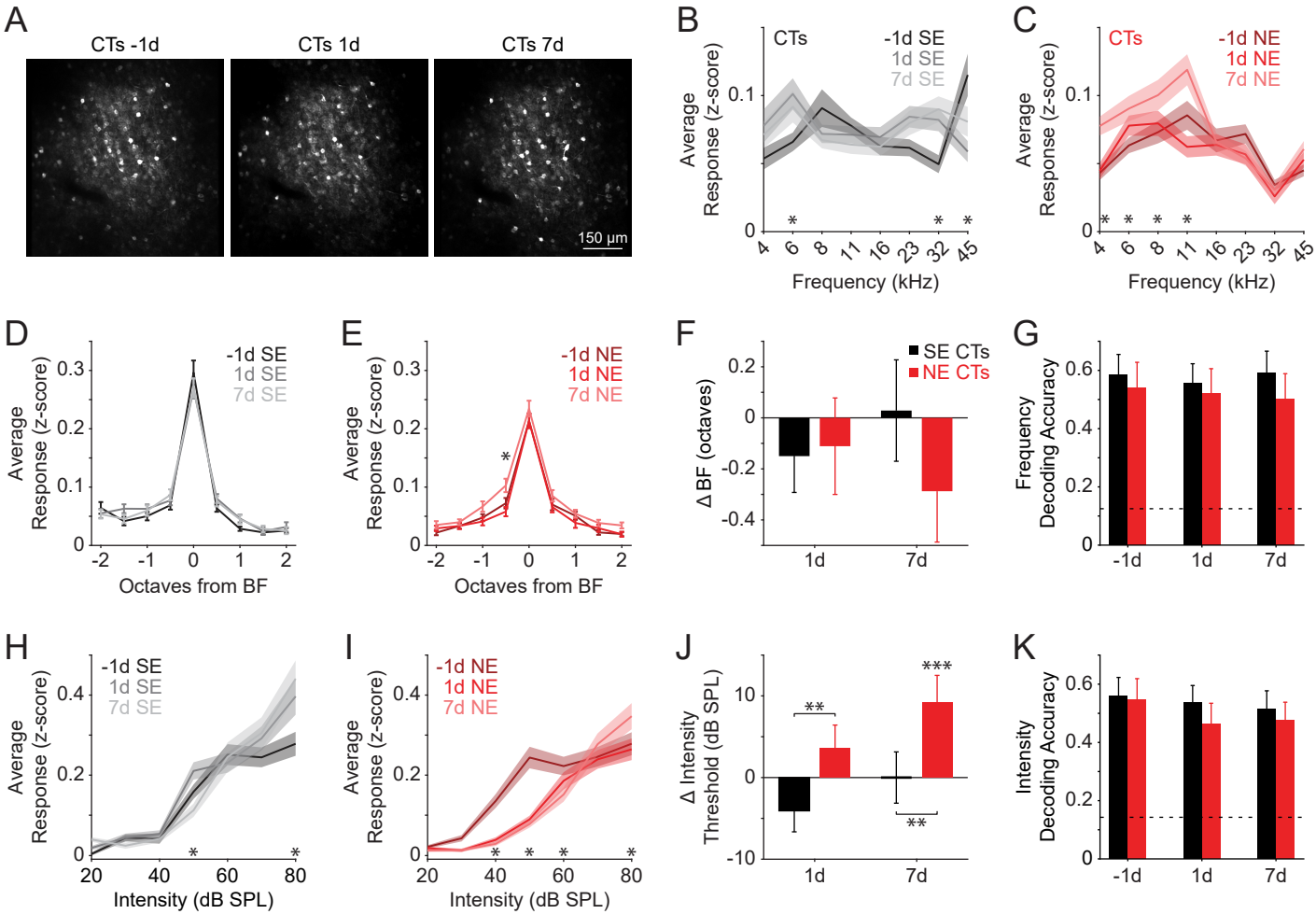
A
CTs -1d
CTs 1d
CTs 7d
150 µm
B
CTs
-1d SE
1d SE
7d SE
Average Response (z-score)
Frequency (kHz)
C
CTs
-1d NE
1d NE
7d NE
Average Response (z-score)
Frequency (kHz)
D
-1d SE
1d SE
7d SE
Average Response (z-score)
Octaves from BF
E
-1d NE
1d NE
7d NE
Average Response (z-score)
Octaves from BF
F
SE CTs
NE CTs
Δ BF (octaves)
1d
7d
G
Frequency Decoding Accuracy
-1d
1d
7d
H
-1d SE
1d SE
7d SE
Average Response (z-score)
Intensity (dB SPL)
I
-1d NE
1d NE
7d NE
Average Response (z-score)
Intensity (dB SPL)
J
Δ Intensity Threshold (dB SPL)
1d
7d
K
Intensity Decoding Accuracy
-1d
1d
7d

Figure 6

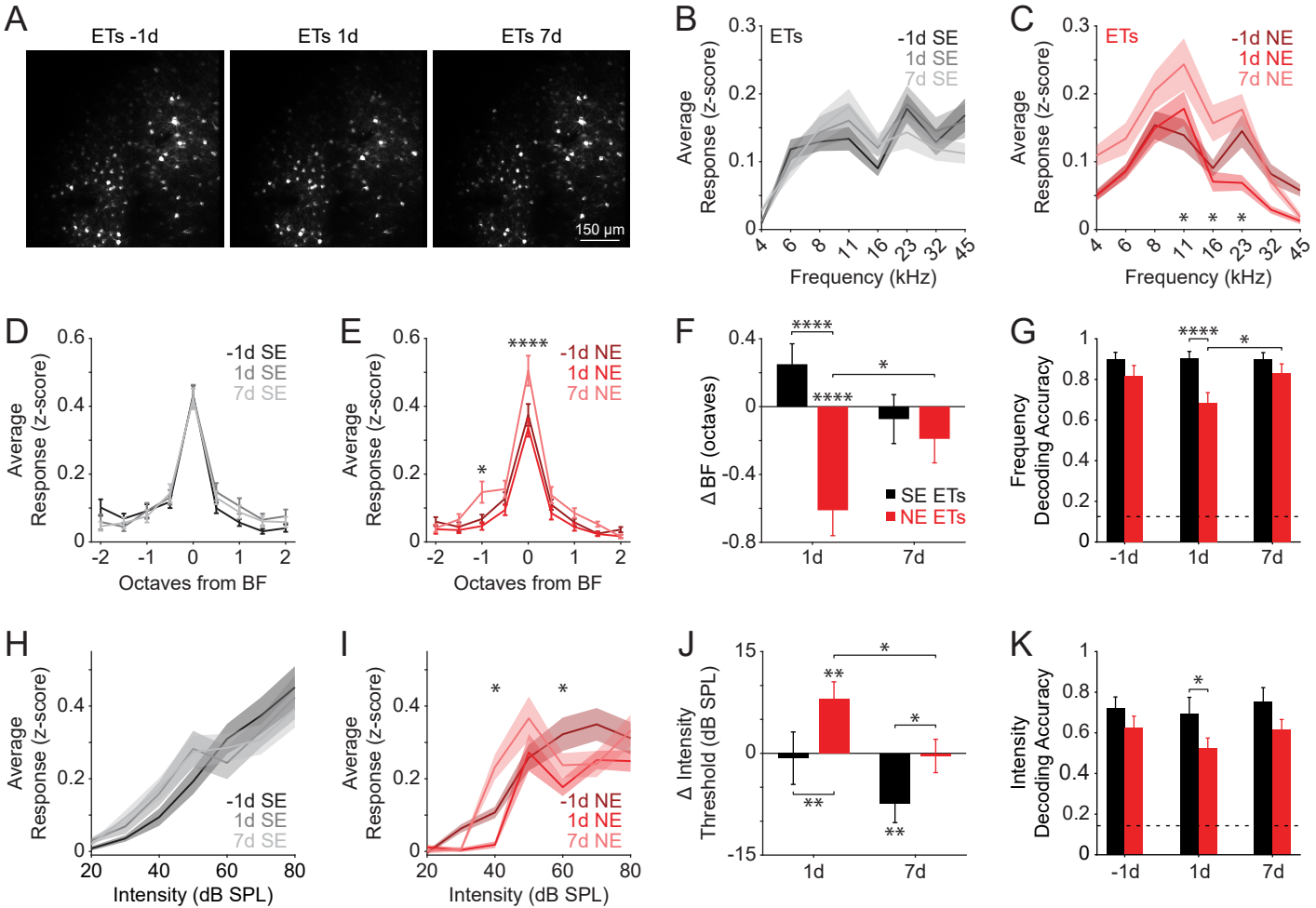
A
ETs -1d
ETs 1d
ETs 7d
150 µm
B
ETs
-1d SE
1d SE
7d SE
Average Response (z-score)
Frequency (kHz)
C
ETs
-1d NE
1d NE
7d NE
Average Response (z-score)
Frequency (kHz)
D
-1d SE
1d SE
7d SE
Average Response (z-score)
Octaves from BF
E
-1d NE
1d NE
7d NE
Average Response (z-score)
Octaves from BF
F
Δ BF (octaves)
SE ETs
NE ETs
1d
7d
G
Frequency Decoding Accuracy
-1d
1d
7d
H
-1d SE
1d SE
7d SE
Average Response (z-score)
Intensity (dB SPL)
I
-1d NE
1d NE
7d NE
Average Response (z-score)
Intensity (dB SPL)
J
Δ Intensity Threshold (dB SPL)
1d
7d
K
Intensity Decoding Accuracy
-1d
1d
7d

Figure 7

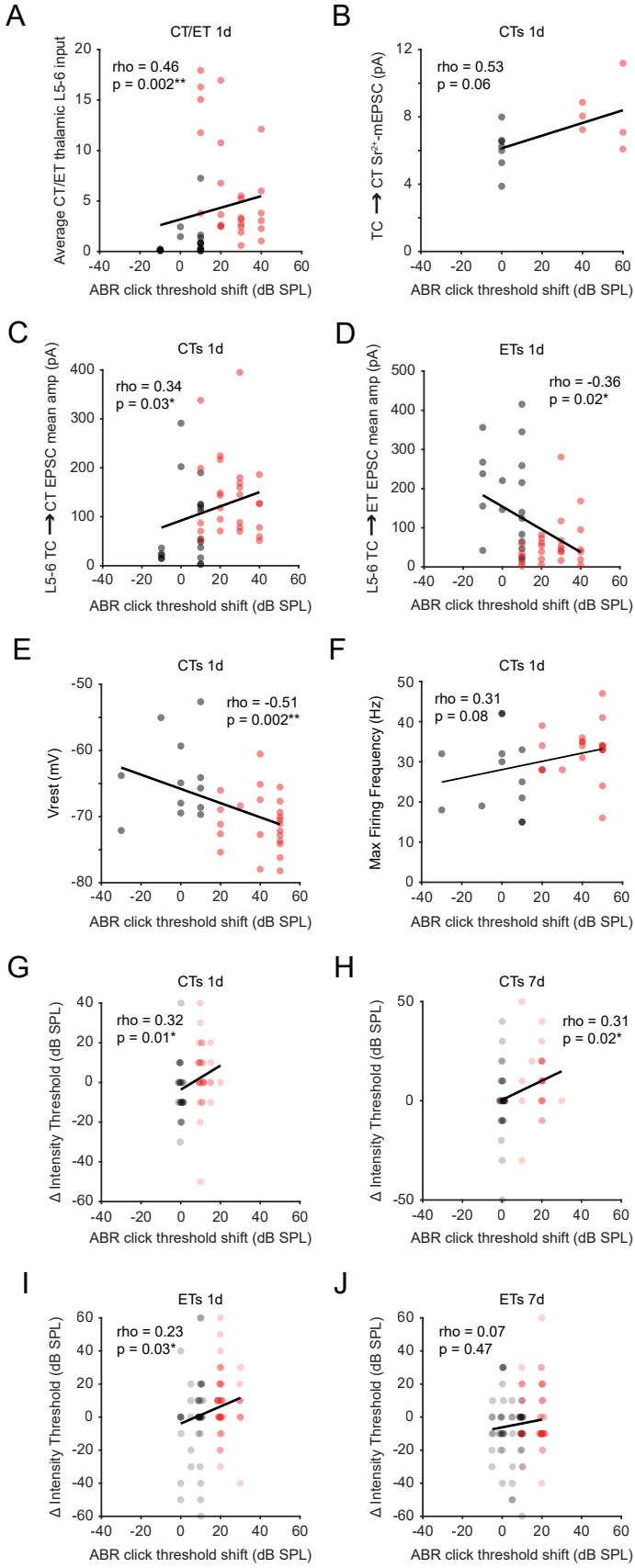
A
CT/ET 1d
rho = 0.46
p = 0.002**
Average CT/ET thalamic L5-6 input
ABR click threshold shift (dB SPL)
B
CTs 1d
rho = 0.53
p = 0.06
TC → CT Sr2+-mEPSC (pA)
ABR click threshold shift (dB SPL)
C
CTs 1d
rho = 0.34
p = 0.03*
L5-6 TC → CT EPSC mean amp (pA)
ABR click threshold shift (dB SPL)
D
ETs 1d
rho = -0.36
p = 0.02*
L5-6 TC → ET EPSC mean amp (pA)
ABR click threshold shift (dB SPL)
E
CTs 1d
rho = -0.51
p = 0.002**
Vrest (mV)
ABR click threshold shift (dB SPL)
F
CTs 1d
rho = 0.31
p = 0.08
Max Firing Frequency (Hz)
ABR click threshold shift (dB SPL)
G
CTs 1d
rho = 0.32
p = 0.01*
Δ Intensity Threshold (dB SPL)
ABR click threshold shift (dB SPL)
H
CTs 7d
rho = 0.31
p = 0.02*
Δ Intensity Threshold (dB SPL)
ABR click threshold shift (dB SPL)
I
ETs 1d
rho = 0.23
p = 0.03*
Δ Intensity Threshold (dB SPL)
ABR click threshold shift (dB SPL)
J
ETs 7d
rho = 0.07
p = 0.47
Δ Intensity Threshold (dB SPL)
ABR click threshold shift (dB SPL)

Figure 8

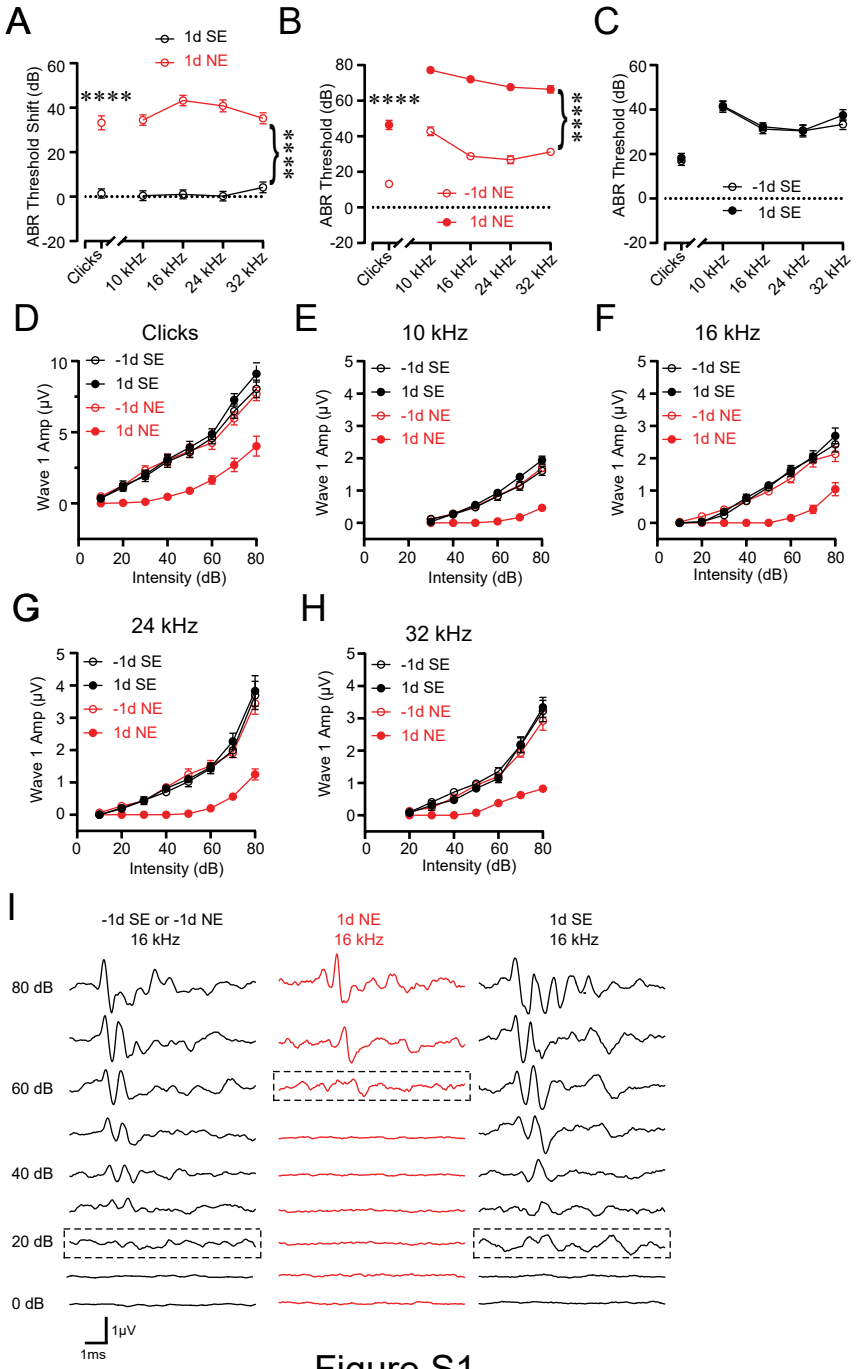
A
1d SE
1d NE
ABR Threshold Shift (dB)
****
****
Clicks
10 kHz
16 kHz
24 kHz
32 kHz
B
ABR Threshold (dB)
****
****
-1d NE
1d NE
C
ABR Threshold (dB)
-1d SE
1d SE
D
Clicks
Wave 1 Amp (μV)
-1d SE
1d SE
-1d NE
1d NE
Intensity (dB)
E
10 kHz
F
16 kHz
G
24 kHz
H
32 kHz
I
-1d SE or -1d NE
16 kHz
1d NE
16 kHz
1d SE
16 kHz
80 dB
60 dB
40 dB
20 dB
0 dB
1μV
1ms

Figure S1

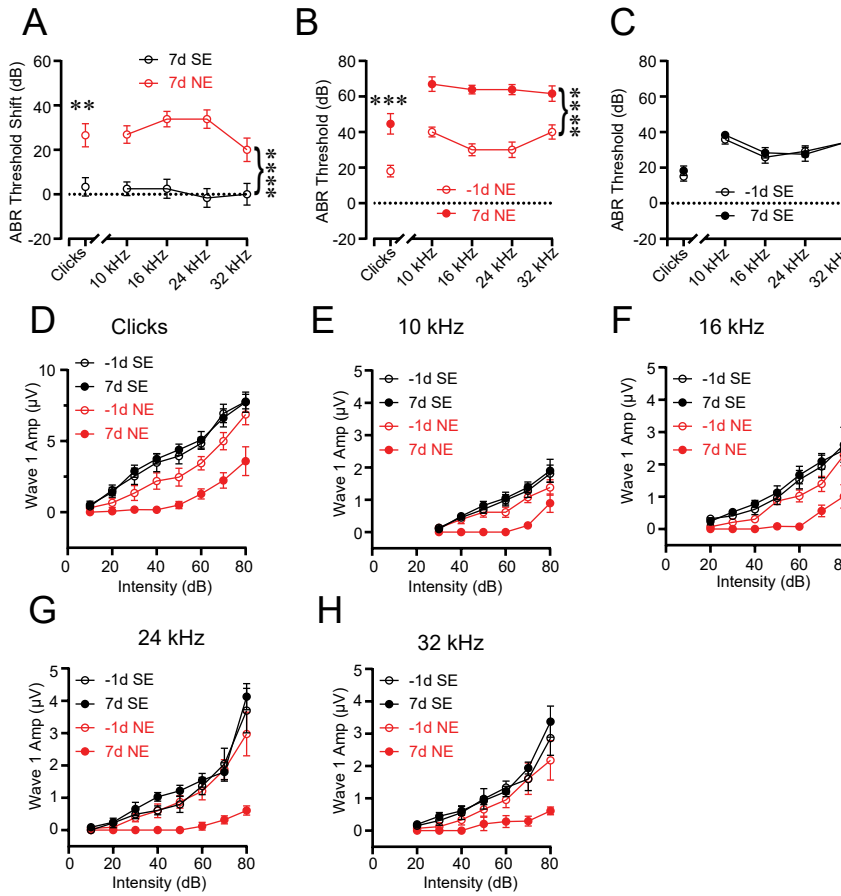
A
B
C
ABR Threshold Shift (dB)
ABR Threshold (dB)
7d SE
7d NE
-1d NE
-1d SE
Clicks
10 kHz
16 kHz
24 kHz
32 kHz
D
E
F
G
H
Wave 1 Amp (µV)
Intensity (dB)

Figure S2

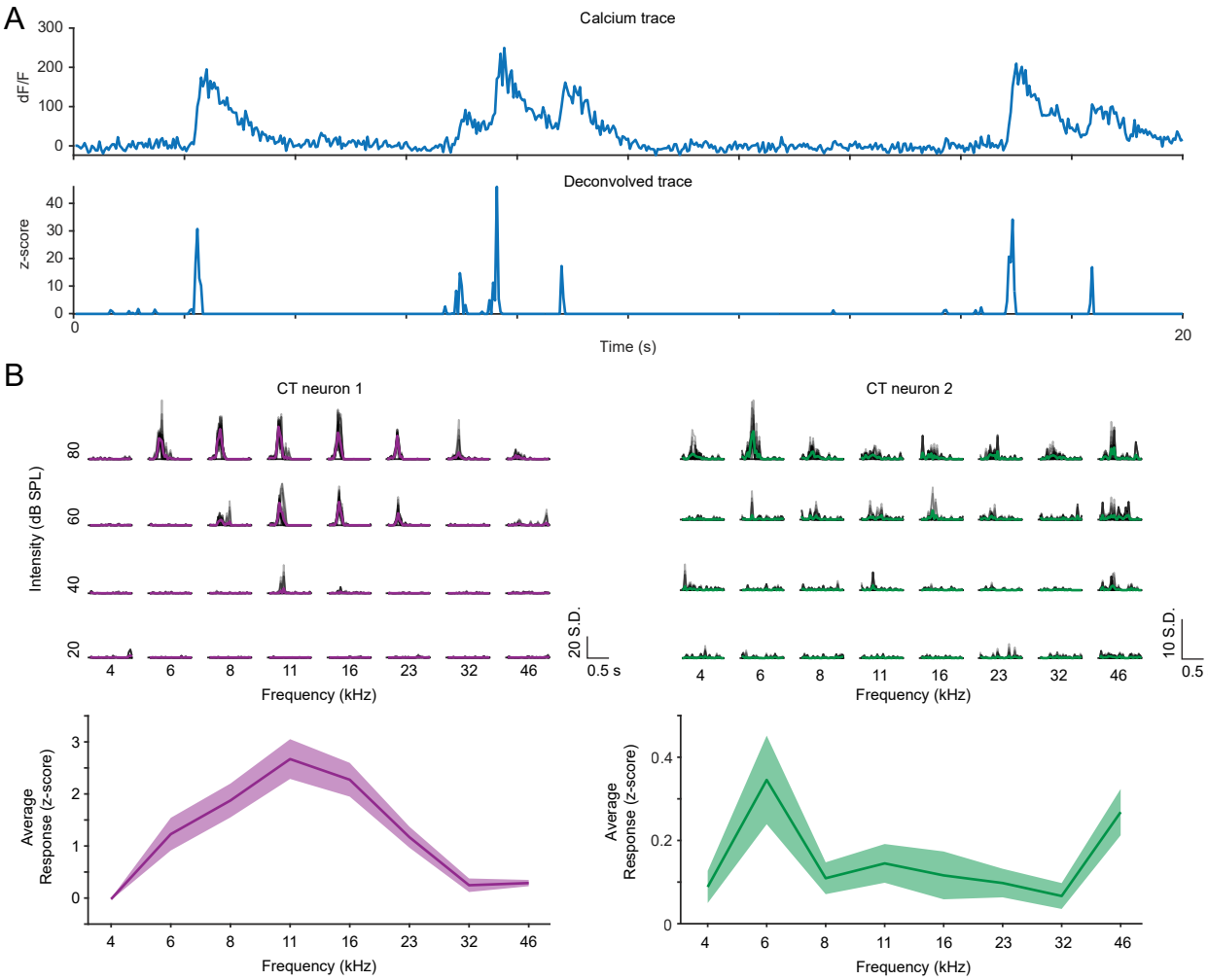
A
Calcium trace
dF/F
300
200
100
0
Deconvolved trace
z-score
40
30
20
10
0
0
20
Time (s)
B
CT neuron 1
CT neuron 2
Intensity (dB SPL)
80
60
40
20
20 S.D.
0.5 s
10 S.D.
0.5 s
4
6
8
11
16
23
32
46
Frequency (kHz)
Average Response (z-score)
3
2
1
0
0.4
0.2

Figure S3

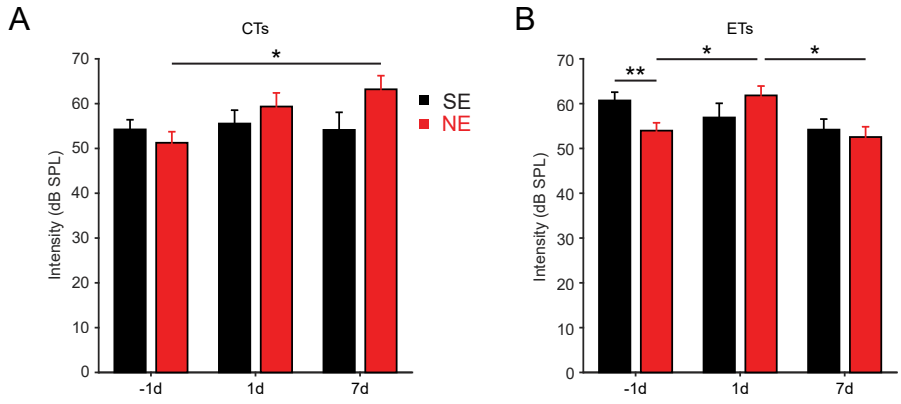
A
CTs
*
SE
NE
Intensity (dB SPL)
70
60
50
40
30
20
10
0
-1d
1d
7d
B
ETs
**
*
*
Intensity (dB SPL)
70
60
50
40
30
20
10
0
-1d
1d
7d

Figure S4

Table 1. Statistical values for Figures 1-7

Figure	Statistical test	Main effect 1	Main effect 2	Interaction effect	N (cells/mice)	Multiple comparison
1D	2-way ANOVA Bonferroni	Exposure: F (1,60) = 5.44 p = 0.023	Day: F (1,60) = 2.25 p = 0.14	F (1,60) = 7.19 p = 0.0095	1d SE: 18/6 1d NE: 26/9 7d SE: 10/6 7d NE: 10/6	1d SE vs 1d NE, p = 0.0002 7d SE vs 7d NE, p > 0.99 1d SE vs 7d SE, p > 0.99 1d NE vs 7d NE, p = 0.021
2A	Unpaired t-test	n/a	n/a	n/a	1d SE: 7/3 1d NE: 6/3	p = 0.037
2C	Unpaired t-test	n/a	n/a	n/a	7d SE: 5/2 7d NE: 6/2	p = 0.68
2E	Mann-Whitney U test	n/a	n/a	n/a	1d SE: 18/6 1d NE: 26/9	p = 0.0042
2G	Unpaired t-test	n/a	n/a	n/a	7d SE: 10/6 7d NE: 10/6	p = 0.94
3A	2-way ANOVA Bonferroni	Exposure: F (1,85) = 0.15 p = 0.70	Day: F (1,85) = 2.26 p = 0.14	F (1,85) = 0.33 p = 0.57	1d SE: 22/8 1d NE: 23/5 7d SE: 23/6 7d NE: 21/4	ns for all groups
3B	2-way ANOVA Bonferroni	Exposure: F (1,85) = 19.81 p < 0.0001	Day: F (1,85) = 9.40 p = 0.0029	F (1,85) = 6.91 p = 0.010	1d SE: 22/8 1d NE: 23/5 7d SE: 23/6 7d NE: 21/4	1d SE vs 1d NE, p < 0.0001 1d SE vs 7d SE, p = 0.0007 1d NE vs 7d NE, p > 0.99 7d SE vs 7d NE, p > 0.99
3C	2-way ANOVA Bonferroni	Exposure: F (1,82) = 3.852 p = 0.0531	Day: F (1,82) = 4.345 p = 0.0402	F (1,82) = 0.0081 p = 0.9284	1d SE: 21/8 1d NE: 21/5 7d SE: 23/6 7d NE: 21/4	1d SE vs 1d NE, p > 0.99 1d SE vs 7d SE, p = 0.95 1d NE vs 7d NE, p = 0.79 7d SE vs 7d NE, p = 0.88
3D	2-way ANOVA Bonferroni	Exposure: F (1,80) = 3.73 p = 0.057	Day: F (1,80) = 0.91 p = 0.34	F (1,80) = 1.26 p = 0.27	1d SE: 21/8 1d NE: 19/5 7d SE: 23/6 7d NE: 21/4	1d SE vs 1d NE, p = 0.23 1d SE vs 7d SE, p > 0.99 1d NE vs 7d NE, p = 0.93 7d SE vs 7d NE, p > 0.99
3F	2-way ANOVA Bonferroni	Exposure: F (1,40) = 9.45 p = 0.0038	Current steps: F (2.431, 97.24) = 155.5 p < 0.0001	F (10,400) = 3.82 p < 0.0001	1d SE: 21/8 1d NE: 21/5	225 pA, p = 0.029 250 pA, p = 0.024 ns for all other groups
3H	2-way ANOVA Bonferroni	Exposure: F (1,42) = 2.64 p = 0.11	Current steps: F (2.369, 99.49) = 208.3 p < 0.0001	F (10,420) = 0.91 p = 0.52	7d SE: 23/6 7d NE: 21/4	ns for all groups
4A	Mann-Whitney U test	n/a	n/a	n/a	1d SE: 5/4 1d NE: 7/5	p = 0.64
4C	Mann-Whitney U test	n/a	n/a	n/a	7d SE: 7/2 7d NE: 5/2	p > 0.99
4E	2-way ANOVA Bonferroni	Exposure: F (1,61) = 8.32 p = 0.0054	Day: F (1,61) = 0.052 p = 0.82	F (1,61) = 4.97 p = 0.030	1d SE: 18/6 1d NE: 26/9 7d SE: 10/6 7d NE: 10/6	1d SE vs 1d NE, p = 0.0002 1d SE vs 7d SE, p > 0.99 1d NE vs 7d NE, p = 0.50 7d SE vs 7d NE, p > 0.99
4G	2-way ANOVA Bonferroni	Exposure: F (1,32) = 1.88 p = 0.18	Day: F (1,32) = 1.43 p = 0.24	F (1,32) = 3.35 p = 0.077	1d SE: 8/3 1d NE: 7/4 7d SE: 9/5 7d NE: 12/4	1d SE vs 1d NE, p > 0.99 1d SE vs 7d SE, p > 0.99 1d NE vs 7d NE, p = 0.23 7d SE vs 7d NE, p = 0.12
5A	2-way ANOVA Bonferroni	Exposure: F (1,81) = 0.27 p = 0.60	Day: F (1,81) = 0.016 p = 0.90	F (1,81) = 1.41 p = 0.24	1d SE: 21/6 1d NE: 21/5 7d SE: 20/5 7d NE: 23/6	ns for all groups
5B	2-way ANOVA Bonferroni	Exposure: F (1,81) = 1.55 p = 0.22	Day: F (1,81) = 0.030 p = 0.86	F (1,81) = 1.55 p = 0.22	1d SE: 21/6 1d NE: 21/5 7d SE: 20/5 7d NE: 23/6	ns for all groups
5C	2-way ANOVA Bonferroni	Exposure: F (1,81) = 3.80 p = 0.055	Day: F (1,81) = 0.014 p = 0.91	F (1,81) = 0.23 p = 0.63	1d SE: 21/6 1d NE: 21/5 7d SE: 20/5 7d NE: 23/6	ns for all groups

5D	2-way ANOVA Bonferroni	Exposure: F (1,81) = 1.60 p = 0.21	Day: F (1,81) = 0.12 p = 0.73	F (1,81) = 0.64 p = 0.43	1d SE: 21/6 1d NE: 21/5 7d SE: 20/5 7d NE: 23/6	ns for all groups
5F	2-way ANOVA Bonferroni	Exposure: F (1,39) = 3.386 p = 0.073	Current steps: F (2.016, 78.63) = 815.9 p < 0.0001	F (14,546) = 1.274 p = 0.22	1d SE: 21/6 1d NE: 20/5	ns for all groups
5H	2-way ANOVA Bonferroni	Exposure: F (1,41) = 0.022 p = 0.88	Current steps: F (2.604, 106.8) = 716 p < 0.0001	F (14,574) = 1.07 p = 0.39	7d SE: 20/5 7d NE: 23/6	ns for all groups
6B	2-Way ANOVA Bonferroni	Frequency: F (7, 11168) = 2.07 p = 0.043	Day: F (2, 11168) = 0.66 p = 0.52	F (14,11168) = 3.68 p < 0.0001	-1d: 507/5 1d: 460/5 7d: 432/5	4 kHz: -1d vs 1d, p = 0.18; -1d vs 7d, p = 0.52; 1d vs 7d, p > 0.99 6 kHz: -1d vs 1d, p = 0.016; -1d vs 7d, p = 0.14; 1d vs 7d, p > 0.99 8 kHz: -1d vs 1d, p = 0.40; -1d vs 7d, p = 0.20; 1d vs 7d, p > 0.99 11 kHz: -1d vs 1d, p > 0.99; -1d vs 7d, p = 0.84; 1d vs 7d, p > 0.99 16 kHz: -1d vs 1d, p > 0.99; -1d vs 7d, p > 0.99; 1d vs 7d, p > 0.99 23 kHz: -1d vs 1d, p = 0.21; -1d vs 7d, p = 0.47; 1d vs 7d, p > 0.99 32 kHz: -1d vs 1d, p = 0.031; -1d vs 7d, p = 0.0052; 1d vs 7d, p > 0.99 45 kHz: -1d vs 1d, p < 0.0001; -1d vs 7d, p = 0.023; 1d vs 7d, p = 0.29
6C	2-Way ANOVA Bonferroni	Frequency: F (7, 15952) = 19.68 p < 0.0001	Day: F (2, 15952) = 11.62 p < 0.0001	F (14,15952) = 2.78 p = 0.0004	-1d:713/8 1d: 638/8 7d: 646/8	4 kHz: -1d vs 1d, p > 0.99; -1d vs 7d, p = 0.0029; 1d vs 7d, p = 0.0064 6 kHz: -1d vs 1d, p = 0.50; -1d vs 7d, p = 0.029; 1d vs 7d, p = 0.73 8 kHz: -1d vs 1d, p > 0.99; -1d vs 7d, p = 0.028; 1d vs 7d, p = 0.16 11 kHz: -1d vs 1d, p = 0.081; -1d vs 7d, p = 0.0041; 1d vs 7d, p < 0.0001 16 kHz: -1d vs 1d, p > 0.99; -1d vs 7d, p > 0.99; 1d vs 7d, p > 0.99 23 kHz: -1d vs 1d, p = 0.46; -1d vs 7d, p = 0.26; 1d vs 7d, p > 0.99 32 kHz: -1d vs 1d, p > 0.99; -1d vs 7d, p > 0.99; 1d vs 7d, p > 0.99 45 kHz: -1d vs 1d, p > 0.99; -1d vs 7d, p = 0.41; 1d vs 7d, p > 0.99
6D	2-Way ANOVA	Frequency: F (8, 8780) = 195.0 p < 0.0001	Day: F (2, 8780) = 0.52 p = 0.59	F (16,8780) = 0.81 p = 0.67	-1d: 507/5 1d: 460/5 7d: 432/5	n/a
6E	2-Way ANOVA Bonferroni	Frequency: F (8, 12876) = 166.4 p < 0.0001	Day: F (2, 12876) = 9.36 p < 0.0001	F (16,12876) = 0.52 p = 0.94	-1d:713/8 1d: 638/8 7d: 646/8	bf-2: -1d vs 1d, p > 0.99; -1d vs 7d, p > 0.99; 1d vs 7d, p > 0.99 bf-1.5: -1d vs 1d, p > 0.99; -1d vs 7d, p > 0.99; 1d vs 7d, p > 0.99 bf-1: -1d vs 1d, p > 0.99; -1d vs 7d, p = 0.43; 1d vs 7d, p = 0.17 bf-0.5: -1d vs 1d, p = 0.67; -1d vs 7d, p = 0.03; 1d vs 7d, p = 0.0007 bf: -1d vs 1d, p > 0.99; -1d vs 7d, p = 0.17; 1d vs 7d, p = 0.17 bf+0.5: -1d vs 1d, p > 0.99; -1d vs 7d, p = 0.58; 1d vs 7d, p = 0.34 bf+1: -1d vs 1d, p = 0.97; -1d vs 7d, p > 0.99; 1d vs 7d, p = 0.62 bf+1.5: -1d vs 1d, p > 0.99; -1d vs 7d, p = 0.65; 1d vs 7d, p > 0.99 bf+2: -1d vs 1d, p > 0.99; -1d vs 7d, p = 0.87; 1d vs 7d, p = 0.87
6F	2-Way ANOVA	Exposure: F(1, 316) = 1.00 p = 0.32	Day: F(2, 316) = 1.14 p = 0.32	F (2,316) = 1.33 p = 0.27	-1d SE: 72/5 1d SE: 40/5 7d SE: 35/5 -1d NE: 99/8 1d NE: 36/8 7d NE: 40/8	n/a
6G	Bootstrap Bonferroni (see Methods)	n/a	n/a	n/a	-1d SE: 507/5 1d SE: 460/5 7d SE: 432/5 -1d NE: 713/8 1d NE: 638/8 7d NE: 646/8	-1d SE vs -1d NE: p = 0.63 1d SE vs 1d NE: p = 0.71 7d SE vs 7d NE: p = 0.40 -1d SE vs 1d SE: p > 0.99 -1d SE vs 7d SE: p > 0.99 1d SE vs 7d SE: p > 0.99 -1d NE vs 1d NE: p > 0.99 -1d NE vs 7d NE: p > 0.99 1d NE vs 7d NE: p > 0.99
6H	2-Way ANOVA Bonferroni	Intensity: F (6, 9142) = 96.27 p < 0.0001	Day: F (2, 9142) = 3.54 p = 0.029	F (12,9142) = 2.51 p = 0.0027	-1d: 438/5 1d: 460/5 7d: 411/5	20 dB: -1d vs 1d, p > 0.99; -1d vs 7d, p = 0.90; 1d vs 7d, p > 0.99 30 dB: -1d vs 1d, p > 0.99; -1d vs 7d, p > 0.99; 1d vs 7d, p > 0.99 40 dB: -1d vs 1d, p > 0.99; -1d vs 7d, p > 0.99; 1d vs 7d, p > 0.99 50 dB: -1d vs 1d, p = 0.38; -1d vs 7d, p = 0.55; 1d vs 7d, p = 0.013 60 dB: -1d vs 1d, p > 0.99; -1d vs 7d, p > 0.99; 1d vs 7d, p > 0.99 70 dB: -1d vs 1d, p = 0.48; -1d vs 7d, p = 0.24; 1d vs 7d, p > 0.99 80 dB: -1d vs 1d, p = 0.0014; -1d vs 7d, p < 0.0001; 1d vs 7d, p = 0.61

6I	2-Way ANOVA Bonferroni	Intensity: F (6, 12453) = 104.6 p < 0.0001	Day: F (2, 12453) = 13.87 p < 0.0001	F (12,12453) = 5.45 p < 0.0001	-1d:636/8 1d: 559/8 7d: 587/8	20 dB: -1d vs 1d, p > 0.99; -1d vs 7d, p > 0.99; 1d vs 7d, p > 0.99 30 dB: -1d vs 1d, p = 0.76; -1d vs 7d, p = 0.77; 1d vs 7d, p > 0.99 40 dB: -1d vs 1d, p = 0.0008; -1d vs 7d, p = 0.0001; 1d vs 7d, p > 0.99 50 dB: -1d vs 1d, p < 0.0001; -1d vs 7d, p < 0.0001; 1d vs 7d, p > 0.99 60 dB: -1d vs 1d, p = 0.50; -1d vs 7d, p = 0.021; 1d vs 7d, p = 0.63 70 dB: -1d vs 1d, p > 0.99; -1d vs 7d, p = 0.69; 1d vs 7d, p = 0.48 80 dB: -1d vs 1d, p > 0.99; -1d vs 7d, p = 0.026; 1d vs 7d, p = 0.0068
6J	2-Way ANOVA Bonferroni	Exposure: F (1, 243) = 14.75 p = 0.0002	Day: F (2, 243) = 4.17 p = 0.017	F (2,243) = 4.94 p = 0.0079	-1d SE: 66/5 1d SE: 27/5 7d SE: 29/5 -1d NE: 71/8 1d NE: 31/8 7d NE: 25/8	-1d SE vs -1d NE: p > 0.99 1d SE vs 1d NE: p = 0.0064 7d SE vs 7d NE: p = 0.0016 -1d SE vs 1d SE: p = 0.27 -1d SE vs 7d SE: p > 0.99 1d SE vs 7d SE: p = 0.45 -1d NE vs 1d NE: p = 0.36 -1d NE vs 7d NE: p = 0.0006 1d NE vs 7d NE: p = 0.14
6K	Bootstrap Bonferroni (see Methods)	n/a	n/a	n/a	-1d SE: 438/5 1d SE: 460/5 7d SE: 411/5 -1d NE: 636/8 1d NE: 559/8 7d NE: 587/8	-1d SE vs -1d NE: p = 0.85 1d SE vs 1d NE: p = 0.38 7d SE vs 7d NE: p = 0.62 -1d SE vs 1d SE: p > 0.99 -1d SE vs 7d SE: p > 0.99 1d SE vs 7d SE: p > 0.99 -1d NE vs 1d NE: p > 0.99 -1d NE vs 7d NE: p > 0.99 1d NE vs 7d NE: p > 0.99
7B	2-Way ANOVA	Frequency: F (7, 9568) = 18.96 p < 0.0001	Day: F (2, 9568) = 0.68 p = 0.51	F (14, 9568) = 1.04 p = 0.41	-1d: 385/5 1d: 414/5 7d: 400/5	n/a
7C	2-Way ANOVA Bonferroni	Frequency: F (7, 6368) = 23.07 p < 0.0001	Day: F (2, 6368) = 19.35 p < 0.0001	F (14, 6368) = 1.93 p = 0.0191	-1d: 268/4 1d: 235/4 7d: 296/4	4 kHz: -1d vs 1d, p > 0.99; -1d vs 7d, p = 0.087; 1d vs 7d, p = 0.098 6 kHz: -1d vs 1d, p > 0.99; -1d vs 7d, p = 0.22; 1d vs 7d, p = 0.23 8 kHz: -1d vs 1d, p > 0.99; -1d vs 7d, p = 0.17; 1d vs 7d, p = 0.13 11 kHz: -1d vs 1d, p = 0.50; -1d vs 7d, p = 0.0003; 1d vs 7d, p = 0.054 16 kHz: -1d vs 1d, p > 0.99; -1d vs 7d, p = 0.039; 1d vs 7d, p = 0.0055 23 kHz: -1d vs 1d, p = 0.020; -1d vs 7d, p = 0.70; 1d vs 7d, p = 0.0003 32 kHz: -1d vs 1d, p = 0.19; -1d vs 7d, p > 0.99; 1d vs 7d, p = 0.38 45 kHz: -1d vs 1d, p = 0.33; -1d vs 7d, p = 0.43; 1d vs 7d, p > 0.99
7D	2-Way ANOVA	Frequency: F (8, 7831) = 99.52 p < 0.0001	Day: F (2, 7831) = 0.58 p = 0.56	F (16, 7831) = 0.58 p = 0.90	-1d: 385/5 1d: 414/5 7d: 400/5	n/a
7E	2-Way ANOVA Bonferroni	Frequency: F (8, 5363) = 98.43 p < 0.0001	Day: F (2, 5363) = 12.03 p < 0.0001	F (16, 5363) = 1.84 p = 0.021	-1d: 268/4 1d: 235/4 7d: 296/4	bf-2: -1d vs 1d, p > 0.99; -1d vs 7d, p > 0.99; 1d vs 7d, p > 0.99 bf-1.5: -1d vs 1d, p > 0.99; -1d vs 7d, p > 0.99; 1d vs 7d, p > 0.99 bf-1: -1d vs 1d, p > 0.99; -1d vs 7d, p = 0.031; 1d vs 7d, p = 0.0064 bf-0.5: -1d vs 1d, p = 0.78; -1d vs 7d, p > 0.99; 1d vs 7d, p = 0.12 bf: -1d vs 1d, p = 0.54; -1d vs 7d, p < 0.0001; 1d vs 7d, p < 0.0001 bf+0.5: -1d vs 1d, p > 0.99; -1d vs 7d, p = 0.96; 1d vs 7d, p = 0.18 bf+1: -1d vs 1d, p > 0.99; -1d vs 7d, p > 0.99; 1d vs 7d, p = 0.49 bf+1.5: -1d vs 1d, p > 0.99; -1d vs 7d, p > 0.99; 1d vs 7d, p > 0.99 bf+2: -1d vs 1d, p > 0.99; -1d vs 7d, p > 0.99; 1d vs 7d, p > 0.99
7F	2-Way ANOVA Bonferroni	Exposure: F (1, 480) = 17.67 p < 0.0001	Day: F (2, 480) = 2.23 p = 0.11	F (2, 480) = 11.34 p < 0.0001	-1d SE: 114/5 1d SE: 68/5 7d SE: 68/5 -1d NE: 111/4 1d NE: 54/4 7d NE: 71/4	-1d SE vs -1d NE: p > 0.99 1d SE vs 1d NE: p < 0.0001 7d SE vs 7d NE: p = 0.40 -1d SE vs 1d SE: p = 0.14 -1d SE vs 7d SE: p > 0.99 1d SE vs 7d SE: p = 0.067 -1d NE vs 1d NE: p < 0.0001 -1d NE vs 7d NE: p = 0.39 1d NE vs 7d NE: p = 0.015

7G	Bootstrap Bonferroni (see Methods)	n/a	n/a	n/a	-1d SE: 385/5 1d SE: 414/5 7d SE: 400/5 -1d NE: 268/4 1d NE: 235/4 7d NE: 296/4	-1d SE vs -1d NE: p = 0.098 1d SE vs 1d NE: p < 0.0001 7d SE vs 7d NE: p = 0.1750 -1d SE vs 1d SE: p > 0.9999 -1d SE vs 7d SE: p > 0.9999 1d SE vs 7d SE: p > 0.9999 -1d NE vs 1d NE: p > 0.9999 -1d NE vs 7d NE: p > 0.9999 1d NE vs 7d NE: p = 0.0360
7H	2-Way ANOVA	Intensity: F (6, 6279) = 44.38 p < 0.0001	Day: F (2, 6279) = 0.2007 p = 0.8182	F (12, 6279) = 0.9433 p = 0.5019	-1d: 331/5 1d: 270/5 7d: 299/5	n/a
7I	2-Way ANOVA Bonferroni	Intensity: F (6, 4879) = 47.49 p < 0.0001	Day: F (2, 4879) = 8.014 p = 0.0003	F (12, 4879) = 2.900 p = 0.0005	-1d: 226/4 1d: 222/4 7d: 252/4	20 dB: -1d vs 1d, p > 0.9999; -1d vs 7d, p > 0.9999; 1d vs 7d, p > 0.9999 30 dB: -1d vs 1d, p = 0.6319; -1d vs 7d, p = 0.6348; 1d vs 7d, p > 0.9999 40 dB: -1d vs 1d, p = 0.1788; -1d vs 7d, p = 0.0191; 1d vs 7d, p < 0.0001 50 dB: -1d vs 1d, p > 0.9999; -1d vs 7d, p = 0.0541; 1d vs 7d, p = 0.1216 60 dB: -1d vs 1d, p = 0.0061; -1d vs 7d, p = 0.1869; 1d vs 7d, p = 0.5673 70 dB: -1d vs 1d, p = 0.1120; -1d vs 7d, p = 0.0510; 1d vs 7d, p > 0.9999 80 dB: -1d vs 1d, p = 0.5423; -1d vs 7d, p > 0.9999; 1d vs 7d, p = 0.2016
7J	2-Way ANOVA Bonferroni	Exposure: F (1, 368) = 11.23 p = 0.0009	Day: F (2, 368) = 6.555 p = 0.0016	F (2, 368) = 3.496 p = 0.0313	-1d SE: 99/5 1d SE: 42/5 7d SE: 50/5 -1d NE: 83/4 1d NE: 49/4 7d NE: 51/4	-1d SE vs -1d NE: p > 0.9999 1d SE vs 1d NE: p = 0.0043 7d SE vs 7d NE: p = 0.0148 -1d SE vs 1d SE: p > 0.9999 -1d SE vs 7d SE: p = 0.0096 1d SE vs 7d SE: p = 0.0806 -1d NE vs 1d NE: p = 0.0068 -1d NE vs 7d NE: p > 0.9999 1d NE vs 7d NE: p = 0.0117
7K	Bootstrap Bonferroni (see Methods)	n/a	n/a	n/a	-1d SE: 331/5 1d SE: 270/5 7d SE: 299/5 -1d NE: 226/4 1d NE: 222/4 7d NE: 252/4	-1d SE vs -1d NE: p = 0.1970 1d SE vs 1d NE: p = 0.0450 7d SE vs 7d NE: p = 0.0910 -1d SE vs 1d SE: p > 0.9999 -1d SE vs 7d SE: p > 0.9999 1d SE vs 7d SE: p > 0.9999 -1d NE vs 1d NE: p > 0.9999 -1d NE vs 7d NE: p > 0.9999 1d NE vs 7d NE: p = 0.4230

Table 2. Statistical values for Supplemental Figures S1-S4

Figure	Statistical test	Main effect 1	Main effect 2	Main effect 3	Interaction effect	N (mice)	Multiple comparison
S1A clicks	Mann-Whitney U test	n/a	n/a	n/a	n/a	1d SE: 24 1d NE: 25	p < 0.0001
S1A frequencies	2-way ANOVA Bonferroni	Exposure: F (1,47) = 235.5 p < 0.0001	Frequency: F (2.598, 122.1) = 2.16 p = 0.11	n/a	F (3,141) = 3.93 p = 0.0099	1d SE: 24 1d NE: 25	p < 0.0001 for all groups
S1B clicks	Mann-Whitney U test	n/a	n/a	n/a	n/a	-1d NE: 25 1d NE: 25	p < 0.0001
S1B frequencies	2-way ANOVA Bonferroni	Exposure: F (1,48) = 388.5 p < 0.0001	Frequency: F (2.855, 137.1) = 27.68 p < 0.0001	n/a	F (3,144) = 3.84 p = 0.011	-1d NE: 25 1d NE: 25	p < 0.0001 for all groups
S1C clicks	Mann-Whitney U test	n/a	n/a	n/a	n/a	-1d SE: 24 1d SE: 24	p = 0.56
S1C frequencies	2-way ANOVA Bonferroni	Exposure: F (1,46) = 0.26 p = 0.61	Frequency: F (2.778, 127.8) = 25.46 p < 0.0001	n/a	F (3,138) = 0.90 p = 0.45	-1d SE: 24 1d SE: 24	ns for all groups
S1D	3-way ANOVA	Exposure: F (1,52) = 20.93 p < 0.0001	Day: F (1,52) = 11.06 p = 0.0016	Intensity: F (2.25,117) = 393.2 p < 0.0001	F (7,364) = 8.59 p < 0.0001	-1d SE: 14 1d SE: 14 -1d NE: 14 1d NE: 14	n/a
S1E	3-way ANOVA	Exposure: F (1,52) = 29.84 p < 0.0001	Day: F (1,52) = 16.36 p = 0.0002	Intensity: F (3.153,163.9) = 314.5 p < 0.0001	F (5,260) = 25.95 p < 0.0001	-1d SE: 14 1d SE: 14 -1d NE: 14 1d NE: 14	n/a
S1F	3-way ANOVA	Exposure: F (1,52) = 31.2 p < 0.0001	Day: F (1,52) = 17.9 p < 0.0001	Intensity: F (2.026,105.3) = 253.9 p < 0.0001	F (7,364) = 8.47 p < 0.0001	-1d SE: 14 1d SE: 14 -1d NE: 14 1d NE: 14	n/a
S1G	3-way ANOVA	Exposure: F (1,52) = 20.63 p < 0.0001	Day: F (1,52) = 16.83 p = 0.0001	Intensity: F (1.636,85.08) = 205 p < 0.0001	F (7,364) = 7.61 p < 0.0001	-1d SE: 14 1d SE: 14 -1d NE: 14 1d NE: 14	n/a
S1H	3-way ANOVA	Exposure: F (1,52) = 28.62 p < 0.0001	Day: F (1,52) = 22.12 p < 0.0001	Intensity: F (2.136,111.1) = 253.8 p < 0.0001	F (6,132) = 11.39 p < 0.0001	-1d SE: 14 1d SE: 14 -1d NE: 14 1d NE: 14	n/a
S2A clicks	Mann-Whitney U test	n/a	n/a	n/a	n/a	7d SE: 12 7d NE: 13	p = 0.0025
S2A frequencies	2-way ANOVA Bonferroni	Exposure: F (1,23) = 32.09 p < 0.0001	Frequency: F (2.194, 50.46) = 3.02 p = 0.053	n/a	F (3,69) = 3.018 p = 0.036	7d SE: 12 7d NE: 13	10 kHz, p = 0.0003 16 kHz, p < 0.0001 24 kHz, p < 0.0001 32 kHz, p = 0.044
S2B clicks	Mann-Whitney U test	n/a	n/a	n/a	n/a	-1d NE: 13 7d NE: 13	p = 0.001
S2B frequencies	Mixed-effects Bonferroni	Exposure: F (1,24) = 47.89 p < 0.0001	Frequency: F (2.801, 65.36) = 3.87 p = 0.015	n/a	F (3,70) = 3.07 p = 0.033	-1d NE: 13 7d NE: 13	10 kHz, p < 0.0001 16 kHz, p < 0.0001 24 kHz, p < 0.0001 32 kHz, p = 0.0063

S2C clicks	Mann-Whitney U test	n/a	n/a	n/a	n/a	-1d SE: 12 7d SE: 12	p = 0.3261
S2C frequencies	2-way ANOVA Bonferroni	Exposure: F (1,22) = 0.060 p = 0.81	Frequency: F (2.435, 53.56) = 7.61 p = 0.0006	n/a	F (3,66) = 0.35 p = 0.79	-1d SE: 12 7d SE: 12	ns for all groups
S2D	3-way ANOVA	Exposure: F (1,20) = 27.6 p < 0.0001	Day: F (1,20) = 4.35 p = 0.0016	Intensity: F (1.954,39.07) = 189 p < 0.0001	F (7,140) = 2.73 p = 0.011	-1d SE: 6 7d SE: 6 -1d NE: 6 7d NE: 6	n/a
S2E	3-way ANOVA	Exposure: F (1,20) = 16.63 p = 0.0006	Day: F (1,20) = 3.69 p = 0.069	Intensity: F (1.852,37.03) = 67.87 p < 0.0001	F (5,100) = 1.54 p = 0.18	-1d SE: 6 7d SE: 6 -1d NE: 6 7d NE: 6	n/a
S2F	3-way ANOVA	Exposure: F (1,20) = 19.92 p = 0.0002	Day: F (1,20) = 3.49 p = 0.077	Intensity: F (2.058,41.15) = 79.58 p < 0.0001	F (6,120) = 1.95 p = 0.078	-1d SE: 6 7d SE: 6 -1d NE: 6 7d NE: 6	n/a
S2G	3-way ANOVA	Exposure: F (1,20) = 15.3 p = 0.0009	Day: F (1,20) = 3.958 p = 0.061	Intensity: F (2.063,41.26) = 85.47 p < 0.0001	F (7,140) = 4.634 p = 0.0001	-1d SE: 6 7d SE: 6 -1d NE: 6 7d NE: 6	n/a
S2H	3-way ANOVA	Exposure: F (1,18) = 13.38 p = 0.0018	Day: F (1,18) = 2.07 p = 0.17	Intensity: F (1.879,33.83) = 54.56 p < 0.0001	F (6,108) = 3.48 p = 0.0035	-1d SE: 6 7d SE: 6 -1d NE: 6 7d NE: 6	n/a
S4A	2-way ANOVA Bonferroni	Exposure: F(1,243) = 1.65 p = 0.20	Day: F(2,243) = 2.57 p = 0.08	n/a	F(2,243) = 2.23 p = 0.11	-1d SE: 66/5 1d SE: 27/5 7d SE: 29/5 -1d NE: 71/8 1d NE: 31/8 7d NE: 25/8	-1d SE vs -1d NE: p = 0.35 1d SE vs 1d NE: p = 0.44 7d SE vs 7d NE: p = 0.074 -1d SE vs 1d SE: p > 0.99 -1d SE vs 7d SE: p > 0.99 1d SE vs 7d SE: p > 0.99 -1d NE vs 1d NE: p = 0.013 -1d NE vs 7d NE: p = 0.018 1d NE vs 7d NE: p > 0.99
S4B	2-way ANOVA Bonferroni	Exposure: F(1,319) = 0.53 p = 0.47	Day: F(2,319) = 2.95 p = 0.054	n/a	F(2,319) = 2.23 p = 0.03	-1d SE: 66/5 1d SE: 42/5 7d SE: 50/5 -1d NE: 67/4 1d NE: 49/4 7d NE: 51/4	-1d SE vs -1d NE: p = 0.012 1d SE vs 1d NE: p = 0.17 7d SE vs 7d NE: p = 0.63 -1d SE vs 1d SE: p = 0.95 -1d SE vs 7d SE: p = 0.17 1d SE vs 7d SE: p > 0.99 -1d NE vs 1d NE: p = 0.016 -1d NE vs 7d NE: p > 0.99 1d NE vs 7d NE: p = 0.021